

AD_____

Award Number: W81XWH-04-1-0229

TITLE: Non-Invasive Monitoring for Optimization of Therapeutic
Drug Delivery by Biodegradable Fiber to Prostate Tumor

PRINCIPAL INVESTIGATOR: Dan Popa, Ph.D.

CONTRACTING ORGANIZATION: The University of Texas at Arlington
Arlington, TX 76019

REPORT DATE: February 2008

TYPE OF REPORT: Final

PREPARED FOR: U.S. Army Medical Research and Materiel Command
Fort Detrick, Maryland 21702-5012

DISTRIBUTION STATEMENT:

Approved for public release; distribution unlimited

The views, opinions and/or findings contained in this report are those of the author(s) and should not be construed as an official Department of the Army position, policy or decision unless so designated by other documentation.

REPORT DOCUMENTATION PAGE				Form Approved OMB No. 0704-0188	
Public reporting burden for this collection of information is estimated to average 1 hour per response, including the time for reviewing instructions, searching existing data sources, gathering and maintaining the data needed, and completing and reviewing this collection of information. Send comments regarding this burden estimate or any other aspect of this collection of information, including suggestions for reducing this burden to Department of Defense, Washington Headquarters Services, Directorate for Information Operations and Reports (0704-0188), 1215 Jefferson Davis Highway, Suite 1204, Arlington, VA 22202-4302. Respondents should be aware that notwithstanding any other provision of law, no person shall be subject to any penalty for failing to comply with a collection of information if it does not display a currently valid OMB control number. PLEASE DO NOT RETURN YOUR FORM TO THE ABOVE ADDRESS.					
1. REPORT DATE 01-02-2008		2. REPORT TYPE Final		3. DATES COVERED 1 Feb 2004 – 31 Jan 2008	
4. TITLE AND SUBTITLE Non-Invasive Monitoring for Optimization of Therapeutic Drug Delivery by Biodegradable Fiber to Prostate Tumor				5a. CONTRACT NUMBER	
				5b. GRANT NUMBER W81XWH-04-1-0229	
				5c. PROGRAM ELEMENT NUMBER	
6. AUTHOR(S) Dan Popa, Ph.D., Email: popa@uta.edu				5d. PROJECT NUMBER	
				5e. TASK NUMBER	
				5f. WORK UNIT NUMBER	
7. PERFORMING ORGANIZATION NAME(S) AND ADDRESS(ES) The University of Texas at Arlington Arlington, TX 76019				8. PERFORMING ORGANIZATION REPORT NUMBER	
9. SPONSORING / MONITORING AGENCY NAME(S) AND ADDRESS(ES) U.S. Army Medical Research and Materiel Command Fort Detrick, Maryland 21702-5012				10. SPONSOR/MONITOR'S ACRONYM(S)	
				11. SPONSOR/MONITOR'S REPORT NUMBER(S)	
12. DISTRIBUTION / AVAILABILITY STATEMENT Approved for Public Release; Distribution Unlimited					
13. SUPPLEMENTARY NOTES Original contains colored plates: ALL DTIC reproductions will be in black and white.					
14. ABSTRACT Chemotherapeutic drugs delivered by systematic administration exhibit great toxicity; patients have to endure suffering from frequent injection or low dose IV treatment. Thus controlled release and of these drugs and real-time monitoring of the effects of the drug can be an better treatment modality. The Hypotheses are (1): A near-infrared (NIR) imager can non-invasively monitor the vascular oxygenation and blood volumes in prostate tumors. (2): The dynamic response of prostate tumor oxygenation to the chronic drug delivery can serve as indicator for treatment prognosis. (3): The control of drug delivery rate will have a significant impact on the treatment prognosis. The specific aims of the of the project are: (1): To design and implement a NIR spectroscopic imaging system. (2): To develop imaging of drug concentration and tumor oxygenation. (3): To control the delivery of drug using a novel implantable micropump (IDDS).(4): To study the relationship between drug release rate, tumor oxygen levels and therapeutic outcome. (5): To create appropriate cancer tumor animal models, that will guide the growth of cancer tumor in Copenhagen rats.					
15. SUBJECT TERMS Technology Development, Radiological Sciences, Tumor Therapy Planning and Prognosis, Tumor Physiology Monitoring.					
16. SECURITY CLASSIFICATION OF:			17. LIMITATION OF ABSTRACT	18. NUMBER OF PAGES	19a. NAME OF RESPONSIBLE PERSON
a. REPORT	b. ABSTRACT	c. THIS PAGE			USAMRMC
U	U	U	UU	72	19b. TELEPHONE NUMBER (include area code)

Table of Contents

Introduction.....	4
Body.....	7
Key Research Accomplishments.....	67
Reportable Outcomes.....	68
References.....	70

2004-2008 Final Report (Years I-IV)

Introduction

Chemotherapeutic drugs delivered by systematic administration exhibit great toxicity; patients have to endure suffering from frequent injection or low dose IV treatment. Thus controlled release of these drugs will be a treatment modality. Moreover, real-time monitoring of the effects of the drug by sensing the dynamic response of the tumor to a particular drug can significantly enhance the therapeutic outcome. The Hypotheses are (1): A near-infrared (NIR) imager can non-invasively monitor the dynamic and chronic distribution of the chemotherapeutic drug, vascular oxygenation, and blood volumes in prostate tumors. (2): The dynamic response of prostate tumor oxygenation to the chronic drug delivery can serve as indicator for treatment prognosis. (3): The control of drug delivery rate will have a significant impact on the treatment prognosis.

This report presents progress and accomplishment during the period between March 1 2005 and January 31 2008. It contains research results from the PI, Dr. Dan Popa, Assistant Professor, Electrical Engineering, UTA, and two co-PI's: Dr. Hanli Liu and Dr. Liping Tang, Professors of BioEngineering Department, UTA. Due to delays in the start of the project and change of PI's, we requested that the project funding be extended for one year, so that remaining research can be completed. Our November 2006 request was approved in February 2007. Also, in September 2007 we sent a revised scope of work request, which was approved as summarized below:

- 1) In January 2005, a change of PI to Dr. Dan Popa has been requested due to the departure of the original PI (Dr. Yueqing Gu) from the United States to People Republic of China .
- 2) After this change, a microfluidic pump was added as a task to the original scope of work, as indicated in our yearly progress reports. The micropump is an alternate method of delivery of cancer drugs to the tumor instead of using drug-coated fibers. The purpose of this document is to request a formal change in the grant SOW for this activity, due to the extensive effort required to complete the micropump work.
- 3) During year 2007-2008 we worked on the packaging of the micropump and testing delivery of cancer drugs.
- 4) Due to the one year delay in research contributions for the PI, more time was needed to construct appropriate animal models and investigate the effectiveness of this drug delivery method in conjunction with cancer cell growth and detection methods. A one-year extension to the grant was approved in February 2007.

Details on SOW change request:

The original aims of the grant were as follows:

(Aim 1): To design and implement a NIR spectroscopic imaging system

(Aim 2): To develop 2D tomographic imaging of drug concentration and tumor oxygenation.

(Aim 3): To control the delivery of drug using both biodegradable fibers.

(Aim 4): To study the relationship between drug release rate, tumor oxygen levels and therapeutic outcome.

(Aim 5): To create appropriate cancer tumor animal models, that will guide the growth of cancer tumor in Copenhagen rats.

During the first 3 years of the grant we investigated the feasibility of NIR tomographic imaging for prostate tumors using transmitted light, light scattering reflectance and autofluorescence, as was indicated in Year III report. We are currently continuing our investigation into cancer detection using this method, but both Aim 1 and Aim 2 remain unchanged.

For Aim 5 we already reported considerable progress in growing tumors in Copenhagen rats. To extend our findings to potential clinical application, part of our research efforts have been placed on the development of drug delivery hydrogel nanoparticles which can locally accumulate in tumor tissue. Hydrogel particles are used because of their good biocompatibility and drug delivery property. To visualize the distribution of these drug eluting nano-devices in animals, these particles were crosslinked with quantum dots which can be observed under fluorescence microscope. Our preliminary results have shown that hydrogel particles preferentially accumulated in the tumor tissue via endocytosis processes. It is our belief that a better understanding of such responses will help the development of better tools to diagnosis and to treat prostate tumor. The specific aim 5 is thus modified to include new study to investigate the property of cancer targeting hydrogel particles.

For Aims 3 and 4 we added a novel method of drug delivery using a novel micropump. This micropump is fabricated using Silicon micromachining technology, and packaged using die bonding technology developed at PI's lab (the Texas Microfactory™). The micropump has been extensively studied using simulation models of increasing complexity, and these models have been used to improve its design. It is hoped that by precisely controlling the amount of cancer drugs delivered to the tumor, side-effects can be minimized and the tumor can be more effectively treated. We request that this change be added to the grant SOW. In particular, we will be investigating models for this micropump to predict the pumping performance, packaging for reliable operation inside the body, and the effect of different drug delivery rates. The importance of this study will shed light on whether implanted micropumps, as opposed to conventional external pumps, are effective for fighting cancer. The main questions we would like to answer are: “

- 1) What do we gain from using low and controlled delivery rates?

- 2) Is the treatment as effective as conventional delivery, but with fewer side-effects?

This knowledge is very valuable for the future development of cancer drug delivery systems. The PI worked closely with the co-PI's to test the micropump in the Life Sciences facility at UTA, to accomplish the following modified SOW:

(Aim 1): To design and implement a NIR spectroscopic imaging system

(Aim 2): To develop 2D tomographic imaging of drug concentration and tumor oxygenation.

(Aim 3 - modified): To control the delivery of drug using a novel implantable micropump (IDDS). Modeling and packaging of the micropump will be undertaken as a significant new activity.

(Aim 4 – modified): To study the relationship between drug release rate, tumor oxygen levels and therapeutic outcome. We study the effects of using different drug delivery rates with a micropump to the effectiveness of the treatment.

(Aim 5 - modified): To create appropriate drug delivery devices and tumor growth models in Copenhagen rats.

Summary of the final report:

At the end of the project, we report the following:

Aims 1,2 and 5 were investigated by co-PI's Liu and Tang as reported in year I, II and III reports (2004-2007). This report contains their findings.

Aims 3 and 4 were investigated by PI Popa and co-PIs Liu and Tang in years II, III, and IV (2005-2008). This report contains their findings, including work performed during the last year of the grant.

Body of Report

Results of research towards Aims 1 and 2 from co-PI Liu

Objective: to design and implement an 8-source, 8-detector, NIR spectroscopic imaging system suitable for dynamic imaging of drug concentrations, tumor oxygenation, and tumor blood volume.

Originally, our aim was to design and implement an 8-source, 8-detector, NIR spectroscopic imaging system. To improve the spatial resolution of the dynamic images, in principle, more sources and detectors are needed. For this purpose, we designed and implemented a CCD-camera based, NIR spectroscopic imaging system, partially because of extra funding that co-investigator (co-I) Liu has obtained. With this new approach, the spatial resolution for dynamic images of tumors under treatment can be improved significantly.

A. CCD Camera Implementation and Calibration

Implementation and Characteristics of the CCD Camera

Since 2004, co-I Liu has closely worked with Apogee Biodimensions, a medical imaging company, to design and implement a multi-spectral, high-speed CCD camera in order to image dynamic light scattering during neural activities. Figure 1 shows a photo of our current CCD camera attached with a mechanical wheel holding six spectral filters at the NIR range. This system allows us to acquire 6-spectral images to quantify both light scattering and absorption of the measured sample.

The spatial resolution of the camera depends on the selection of the field of view; the typical pixel size in our study is about $20 \times 20 \mu\text{m}^2$. To statistically smoothen out the random noise due to Brownian motion of various scatterers in tissue, we can bin multiple pixels for a local point reading to achieve a sub-mm spatial resolution. The temporal resolution of our current camera, on the other hand, is ~ 50 ms per image frame if a fixed filter is chosen and utilized. By choosing a smaller region of interest, the image acquisition rate can be improved further to obtain 20 ms per frame. When the six filters are utilized, the complete cycle of 6 spectral images takes ~ 15 seconds. We normally take multi-spectral images during the baseline recording time to obtain static values of both light scattering and absorption parameters.

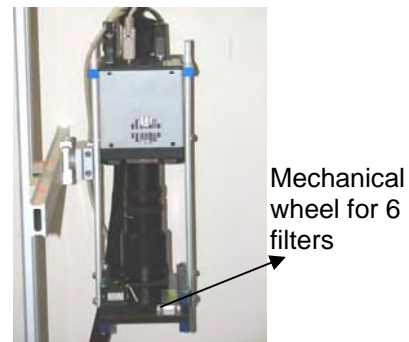


Figure 1. A fast 12-bit CCD camera with a mechanical wheel attached at the camera head.

Laboratory Calibration for Determination of Light Scattering and Absorption from the CCD Camera

In order to separate the effects between light scattering from absorption for the CCD imaging data, we developed an empirical approach. We can start with eq. (1) for the light reflectance taken from the CCD camera:

$$R(\mu_a, \mu_s') = \frac{\Psi(I_0, \mu_s') \cdot (\mu_s')^2}{4\pi} \exp(-z_0 \mu_{eff}) \quad (1)$$

where μ_a and μ_s' are light absorption and scattering coefficients, $\mu_{eff} = (3\mu_a\mu_s')^{0.5}$, $z_0 = 1/\mu_s'$, and $\Psi(I_0, \mu_s') = \Psi_{CCD}(I_0, \mu_a, \mu_s')$ is the calibration term for the CCD camera and needs to be obtained from the laboratory phantom measurements. In our previous study for a needle probe, we proved that $\Psi(I_0, \mu_a, \mu_s')$ is a function of only μ_s' , not strongly depending on absorption. For CCD camera calibration, we performed the experiments as described below:

- 3 liters of intralipid solution in a large container were imaged using the multi-wavelength CCD camera. The images were obtained for the following intralipid concentrations: 0.5 %, 0.8 %, 1.0%, 1.2%, 1.5%, and 2.0% and also 1.0% intralipid with 1.0, 1.5, and 2.0 ml of ink or (horse blood) mixed with it, as shown in Figures 2(a) and 2(b). Optical parameters of the solution, μ_a and μ_s' , from a standard spectrometer (the ISS oximeter) were obtained before imaging. The camera was mounted on top of the solution and a light from a broadband light source was focused on the intralipid solution in such a way that there is uniform illumination. Care was taken to mark the height between the camera entrance and the surface of the liquid. This was to ensure that there was no difference in successive experiments and it was easily repeatable. The camera was then adjusted (e.g., focus distance and slit width) to obtain a clear image of the intralipid solution. 10 images from a particular filter were taken, and all images were obtained at the same integration time (90ms).

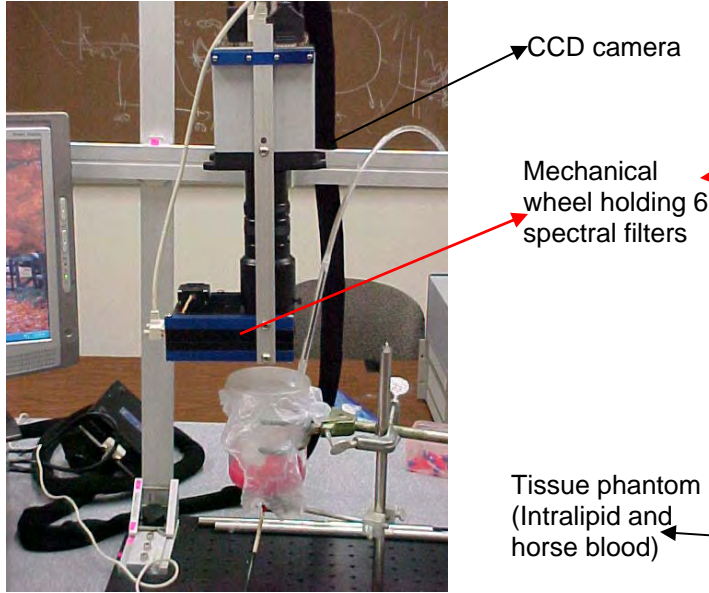


Figure 2(a) Experimental setup of the CCD camera for the laboratory phantom study.



Figure 2(b) A close look of the CCD camera head with the Intralipid solution mixed with horse blood.

After the CCD readings were recorded, we averaged them across the entire images, as functions of μ_a and μ_s' by measuring ink and Intralipid concentrations,

respectively. Figures 3(a) and 3(b) show that $\Psi_{CCD}(I_0, \mu_a, \mu_s')$ has an power dependence on μ_s' and a linear relationship on μ_a .

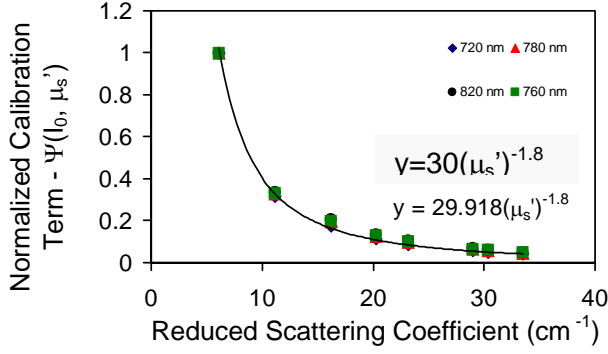


Figure 3(a) The empirical relationship between $\Psi_{CCD}(I_0, \mu_a, \mu_s')$ and μ_s' , having a power of $(\mu_s')^{-1.8}$.

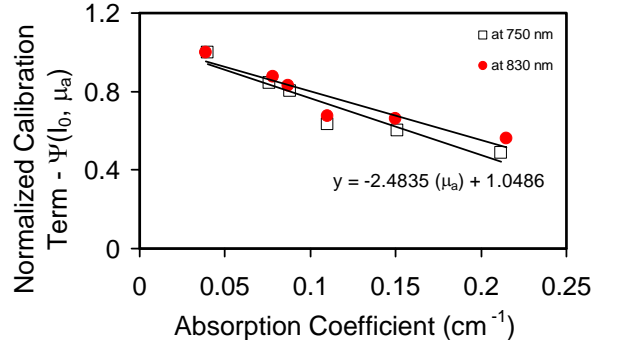


Figure 3(b) The empirical relationship between $\Psi_{CCD}(I_0, \mu_a, \mu_s')$ and μ_a , having a linear relationship.

Based on the preliminary results given above, we then express $\Psi_{CCD}(I_0, \mu_a, \mu_s')$ as

$$\Psi_{CCD}(I_0, \mu_a, \mu_s') = f(\mu_s') g(\mu_a) = \alpha (\mu_s')^{-1.8} (\mu_a + \beta), \quad (2)$$

where α and β are two empirical parameters that can be calibrated from the laboratory phantoms and be later utilized for quantification of μ_a and μ_s' of the rat prostate tumors so as to quantify hemodynamic responses to the therapy.

Co-investigator Liu has also conducted a comparison study to quantify absolute hemodynamic parameters using a spectroscopic approach on rat prostate tumors. Such a quantitative method will lead to better accuracy for the 2D tomographic images in monitoring effects of prostate tumor treatments.

B. Quantification of absolute hemodynamic parameters in rat prostate tumors in vivo

We have utilized a hand-held, spectroscopic probe by selecting multiple appropriate separations between the source and detectors. The following figures show our current hand-held, multi-channel optical probe (Fig. 4a) and its cross-section with dimension (Fig. 4b), the entire optical system with the multi-channel CCD spectrometer (Fig. 5), and the probe being used to measure the spectral readings from a rat prostate tumor (Fig. 6).



Fig. 4a

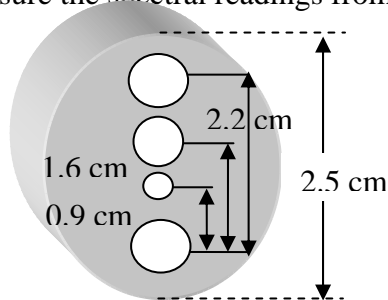


Fig.4b

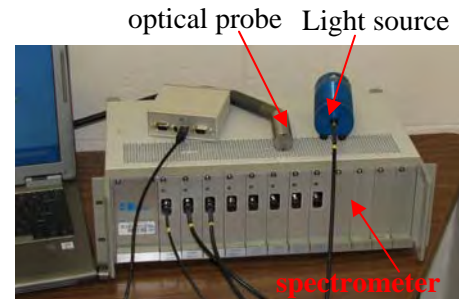


Fig. 5

The current hand-held, multi-channel optical probe has source-detector separations of 0.4, 0.8, 1.2 cm in order to interrogate several depths of prostate tissue. The multi-detecting channels are connected to a multi-channel, CCD-array spectrometer to obtain spectroscopic readings. After the probe and the spectrometer were calibrated, we have conducted the laboratory phantom testing to investigate the spectroscopic features of tissues which have different hemodynamic parameters. Then, we utilized the calibrated, multi-channel, optical probe to obtain data from rat prostate tumors.



Fig. 6

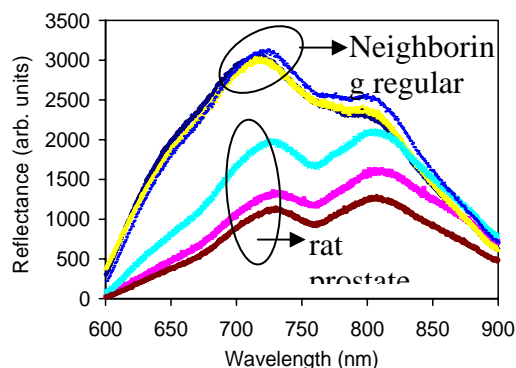


Fig. 7

Figure 7 shows several spectra taken from three rat prostate tumors using the optical probe and the setup shown in Fig. 6. To make a comparison between the spectra taken from the tumors and from the neighboring tissues, we have also measured the spectra of regular neighboring tissues from the same rats. The spectra of regular tissues clearly demonstrate great distinction from those of tumor tissues, as plotted also in Figure 7.

C. Light-scattering reflectance and auto-fluorescence from rat prostate tumor in vivo

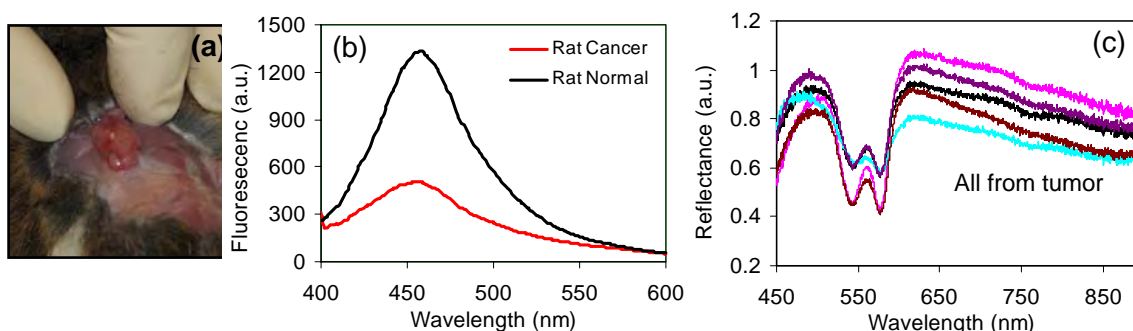


Figure 8. Photo of (a) an exposed living prostate tumor on the rat fore back. Both (b) steady-state autofluorescence and (c) light-scattering reflectance were taken from the exposed rat tumor to avoid the skin effect.

Co-PI Liu has developed a rat prostate tumor model, under the support from the DOD Prostate Research Program, using adult male Copenhagen rats that were implanted with prostate carcinoma on the fore back (Figs. 8a and 8b). We have conducted our preliminary experiments on the animal tumors of light scattering reflectance (Fig. 7) and

autofluorescence (Fig. 8d) using a needle-like probe, as well as the diffuse light reflectance with the multi-channel probe.

D. Auto-fluorescence lifetime of rat prostate tumor measured in vitro

Co-I Liu has recently collaborated with Dr. Gryczynskis from the University of North Texas Health Science Center at Fort Worth, who has applied the time-resolved technique to investigate the auto fluorescence lifetime of the rat prostate tumor tissues compared to the normal muscle tissues. Both types of tissues were removed from the rats a few hours before the measurements. The main advantage of the time-resolved fluorescence is that such measurements reveal intrinsic fluorophore photophysics parameters, which are intensity independent. For these preliminary measurements, we used a FluoTime200 fluorometer (PicoQuant, Inc.) equipped with pulsed light sources. Firstly, we were not sure that a weak pulsed laser would provide enough power to efficiently excite the tissue autofluorescence. Secondly, we did not know if the changes in observed lifetimes would be sufficient to distinguish the tumor samples from the normal. We selected the excitation of 375 nm hoping for efficient NADH/Flavins excitation.

We were positively surprised to detect strong fluorescence signals in the visible region of 440-550 nm. We could attenuate the signal by 100 fold using a neutral density filter with OD=2, and still collect high quality lifetime data. Thus, we do not expect any problem with the autofluorescence data collection in future time-resolved “Field” measurements in vivo.

An example of the time-resolved tissue autofluorescence is presented in Figure 9, where the red and black curves result from the normal and prostate tumor tissues, respectively. The blue sharp spike is the instrument response function. This figure clearly shows a significant lifetime decrease in tumor tissue.

The autofluorescence intensity decays of the tissue can be approximated with the multi-exponential model, as given:

$$I(t) = \sum \alpha_i \exp(-t/\tau_i) \quad (3)$$

where τ_i are the decay times, α_i represent the amplitudes of the components at $t=0$. In this case, three components ($n=3$) were sufficient to fit the data with an acceptable confidence. The fractional contributions f_i of each decay time to the steady-state intensity is given by

$$f_i = \alpha_i \tau_i / \sum \alpha_j \tau_j. \quad (4)$$

Then, the average lifetime for multi-exponential decay is given by $\tau = \sum f_i \tau_i$. Another quantity, called amplitude-weighted lifetime, is given by $\langle \tau \rangle = \sum \alpha_i \tau_i$, which is proportional to the area under the curve.

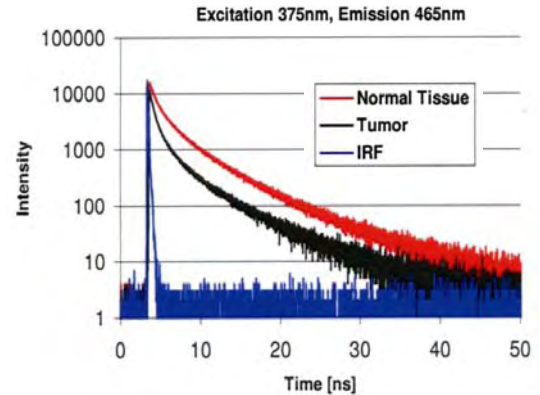


Fig. 9 Time-resolved auto-fluorescence data from both rat tumor and normal tissues.

The following Table provides a list of lifetime parameters analyzed using eqs. (3) and (4).

Observation (465 nm)	α_1	τ_1 (ns)	α_2	τ_2 (ns)	α_3	τ_3 (ns)	$\langle\tau\rangle$ (ns)	τ (ns)	χ_R^2
Normal	0.62	0.53	0.30	2.22	0.08	6.52	1.53 ^{α)}	3.36 ^{β)}	1.19
Tumor	0.73	0.35	0.22	1.51	0.05	5.83	0.86	2.49	1.01

α) $\langle\tau\rangle = \sum \alpha_i \tau_i$; β) τ is the average lifetime and equal to $\sum f_i \tau_i$, $f_i = (\alpha_i \tau_i) / (\sum \alpha_i \tau_i)$

This table unambiguously demonstrates that both amplitude weighted lifetime and average lifetime, i.e., $\langle\tau\rangle$ and τ , are significantly different between the normal muscle tissue and prostate tumor tissue. This knowledge implies that both $\langle\tau\rangle$ and τ may be used as classification markers to identify prostate tumor from normal tissues. In short, we learned in this preliminary time-resolved study that decays in autofluorescence intensity from prostate cancer are easily detectable, and that time-resolved autofluorescence of the tissue is durable, carrying characteristic information on cancer. We are confident that a portable device for “Field” lifetime measurements can be constructed with a modest cost.

E. NIRs of Rat Prostate Tumor in Vivo

We have inspected the data in the NIR region up to 1100 nm so as to examine the signals at dominant water absorption. Figure 10 plots apparent absorption, which is calculated by taking the logarithm of reciprocal reflectance. This experimental result clearly demonstrates that the prostate tumor has lower water and higher deoxy-hemoglobin concentrations than normal tissues, in good agreement with the report by Alfano et al [42].

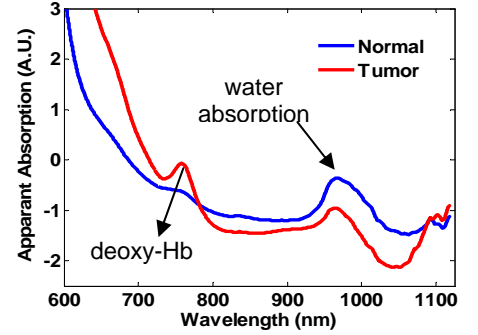


Fig. 10: Log of reciprocal reflectance

F. Algorithm Development to Quantify Hemodynamic Parameters for Rat Prostate Tumors

Light propagation in tissues is dominated by absorption and scattering phenomena. The scattering in tissue is known to be highly forward, depending on the anisotropy parameter. The light fluence in tissues can be obtained from radiative transport equation with certain assumptions [43]. Using Green’s function as the solution to diffusion approximation, diffuse reflectance as a function Z_0 and source-detector separation ‘ ρ ’ is given as

$$R(\rho, Z_0) = \frac{1}{4\pi} \left[Z_0 \left(\mu_{eff} + \frac{1}{r_1} \right) \frac{e^{-\mu_{eff} r_1}}{r_1^2} + Z_0 + 2Z_b \left(\mu_{eff} + \frac{1}{r_2} \right) \frac{e^{-\mu_{eff} r_2}}{r_2^2} \right] \quad (5)$$

where $Z_0 = 1/\mu_t = 1/(\mu_a + \mu_s')$, $r_1 = \sqrt{Z_0^2 + \rho^2}$, $r_2 = \sqrt{(Z_0^2 + 4AD)^2 + \rho^2}$, $\mu_{eff} = \frac{\mu_a}{D}$, $D = 1/3(\mu_a + \mu_s')$.

The major absorbing chromophores in tissue in the NIR wavelength range are oxygenated and deoxygenated hemoglobin and water to an less extent . These chromophores have distinct optical signatures in this wavelength region. The absorption coefficient in the NIR region can be written as

$$\mu_a(\lambda) = [HbO_2] \cdot \epsilon_{HbO_2}(\lambda) + [Hb] \cdot \epsilon_{Hb}(\lambda) + \%H_2O \cdot \epsilon_{H_2O}(\lambda), \quad (6)$$

where $[HbO_2]$ and $[Hb]$ represent molar concentrations of oxygenated and deoxygenated hemoglobin; ϵ_{HbO_2} , ϵ_{Hb} and ϵ_{H_2O} are extinction coefficients for oxygenated, deoxygenated hemoglobin and water, respectively [44]; λ denotes a wavelength within the NIR region. The reduced scattering coefficient can be approximated as

$$\mu_s'(\lambda) = -c \cdot \lambda + d \quad (7)$$

where c and d are tissue-dependent parameters.

The diffusion approximation in Eq.5 is used to generate forward data (reflectance spectra). Simulated diffuse reflectance spectra obtained at different hemoglobin oxygen saturation levels show a strong spectral dependence on oxygenation levels.

F1. Second differential NIRS

We made the use of second-differential spectroscopy to determine concentrations of deoxygenated hemoglobin relative to tissue water concentration by fitting the spectral features of these two chromophores in the wavelength range of 710 nm to 780 nm [45]. This is used as prior information in the optimization algorithm to obtain reduced scattering coefficients and concentrations of oxygenated hemoglobin.

F2. Optimization method

The inverse calculation for reduced scattering coefficients and concentrations of oxygenated hemoglobin is treated as an optimization problem, and hence the solution lies in determining those values of $[HbO_2]$, $[Hb]$, c , and d , as given in eqs. (6) and (7), in such a way that the objective function, χ^2 , is minimized in error, as given below:

$$\chi^2 = \sum_{i=1}^n (\varphi_{measured} - \varphi_{predicted})^2, \quad (6)$$

where $\varphi_{measured}$ is the reflectance spectrum obtained from the turbid medium, and $\varphi_{predicted}$ is the reflectance spectrum calculated from eq. (3) using assumed values of μ_a and μ_s' at each wavelength. Then Ant Colony optimization algorithm [46] is used to iteratively optimize the parameters of $[HbO_2]$, $[Hb]$, c , d and hence the hemoglobin derivative concentrations and reduced scattering coefficients.

In the process of optimization, two normalization approaches were used. Firstly, the measured spectral reflectance was normalized to scale of 0-1, followed by initial

determination of reduced scattering coefficient and blood oxygen saturation. Using the determined parameters as initial or prior information, all parameters including water concentration were further optimized with the second normalization approach, where all reflectance values were normalized by the reflectance values measured at 600 nm.

F3. Experimental Setup for Validation

Fig. 11 shows the experimental arrangement for steady-state, optical reflectance measurements during the phantom study. Light from the light source (Illumination Technologies, Inc. Model 3900 DC regulated, Light Feedback Fiber Optic Light source) was delivered via an optical fiber (Innova Quartz Inc, Phoenix, Arizona, 3-mm core diameter, SMA) to the surface of the sample and collected at a distance 3 cm away from the source. The collected light was delivered to a CCD array spectrometer (Ocean Optics Inc, Florida, S2000 Spectrometer (350-1050 nm), 200 μm slit width). The spectrum of the light source was measured separately by shining light from the source fiber on a standard reflectance sample (Labsphere Inc) and the reflected light collected with the detector fiber. Relative reflectance was calculated to be the sample spectrum divided by the source spectrum. Both measurements used the same delivery fiber, collection fiber, and detector apparatus. Acquisition time per sample for reflectance measurements was of the order of 30-200 milliseconds. The ISS oximeter probe was also placed on the same homogenous sample at another location for comparison and validation. The phantom was a mixture of defibrinated horse blood (Hemostat Labs Inc, Dixon, CA) and an aqueous scattering suspension Intralipid (20%, Kabi Pharmacia, Inc).

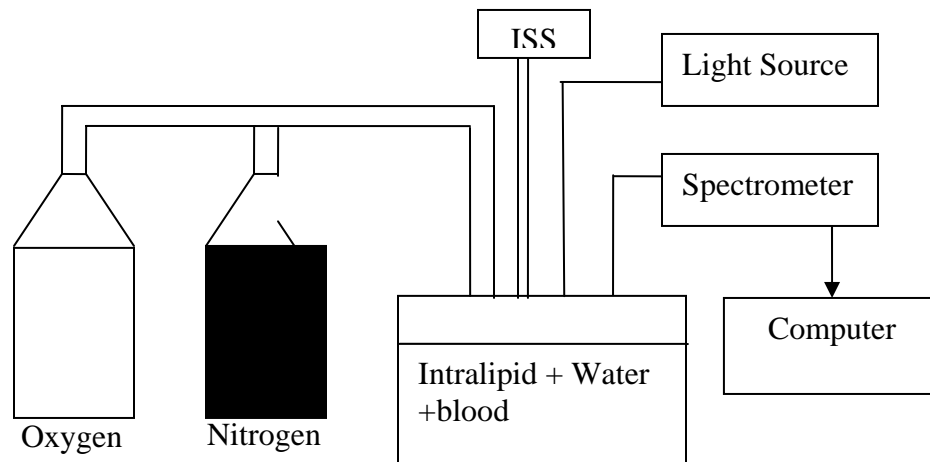


Fig. 11. Schematic diagram of experimental setup used for the in vitro measurement of reflectance spectra from a liquid tissue phantom. It shows the configuration of light source and detectors. The source-detector separation was 3 cm. The gas tubing was connected to the oxygen tank to oxygenate and to a nitrogen tank to deoxygenate the solution. The ISS Oximeter was used for the measurement of absolute concentrations of hemoglobin derivatives and reduced scattering coefficients.

F5. Experimental Results for Validation

Figures 12(a) and 12(b) display the raw spectra and the corresponding attenuation spectra, respectively, taken from an oxygenated and deoxygenated state of a blood intralipid phantom.

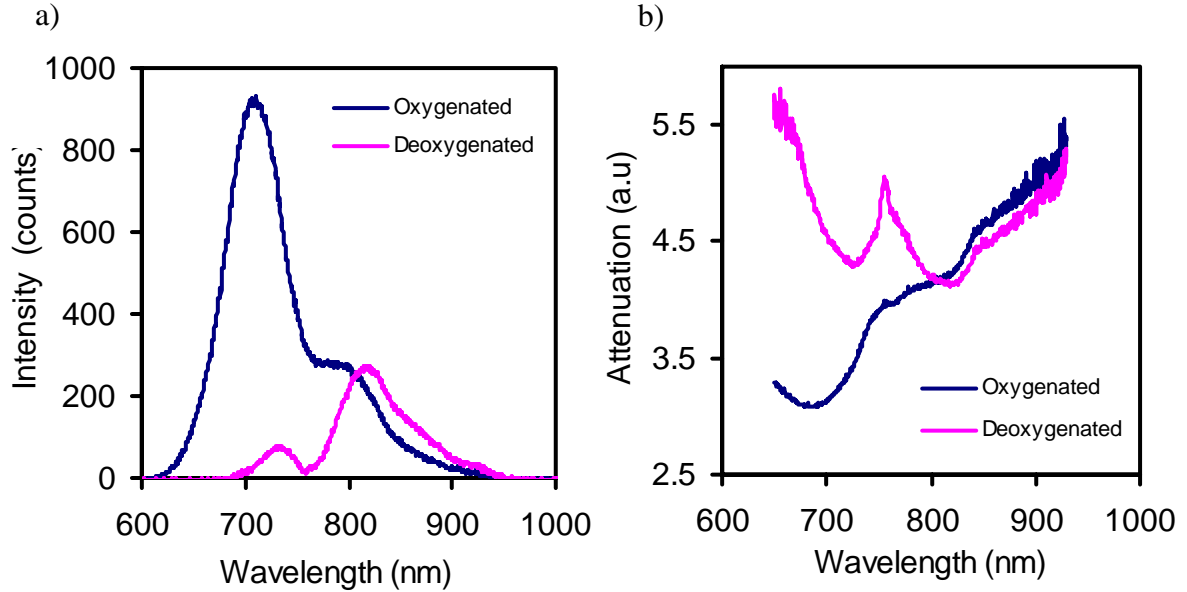


Figure 12 Reflectance (a) and attenuation (b) spectra acquired from blood-intralipid phantoms. The oxygenated state and deoxygenated state have high (95%) and low (37%) blood oxygen saturation levels.

The reflectance spectrum measured from the oxygenated state shows significantly higher intensities in range of 600-800 nm than those obtained in the deoxygenated state. These features are typical spectral features of HbO and Hb. The behavior is vice-versa in the wavelengths of 800-950 nm. The attenuation spectra being reciprocals of corresponding reflectance spectra show complimentary behaviors.

The second derivatives of the attenuation spectra are determined as described in section F1. The second differential spectrum from the measurements is fit with reference spectra to obtain concentrations of Hb relative to tissue water.

Second derivative spectra for the corresponding deoxygenated state and oxygenated state of the phantom are shown in Figure 13(a) and Figure 13(b) respectively. The magnitude of the second derivative is lower by a factor of 10 for the oxygenated state as compared with deoxygenated state. The distinct spectral feature of Hb (a trough at 760 nm) is seen in Figure 13(a) but not present in Figure 13(b). $[Hb]$ determined from fitting the second differential spectra are used as a priori information for the optimization algorithm.

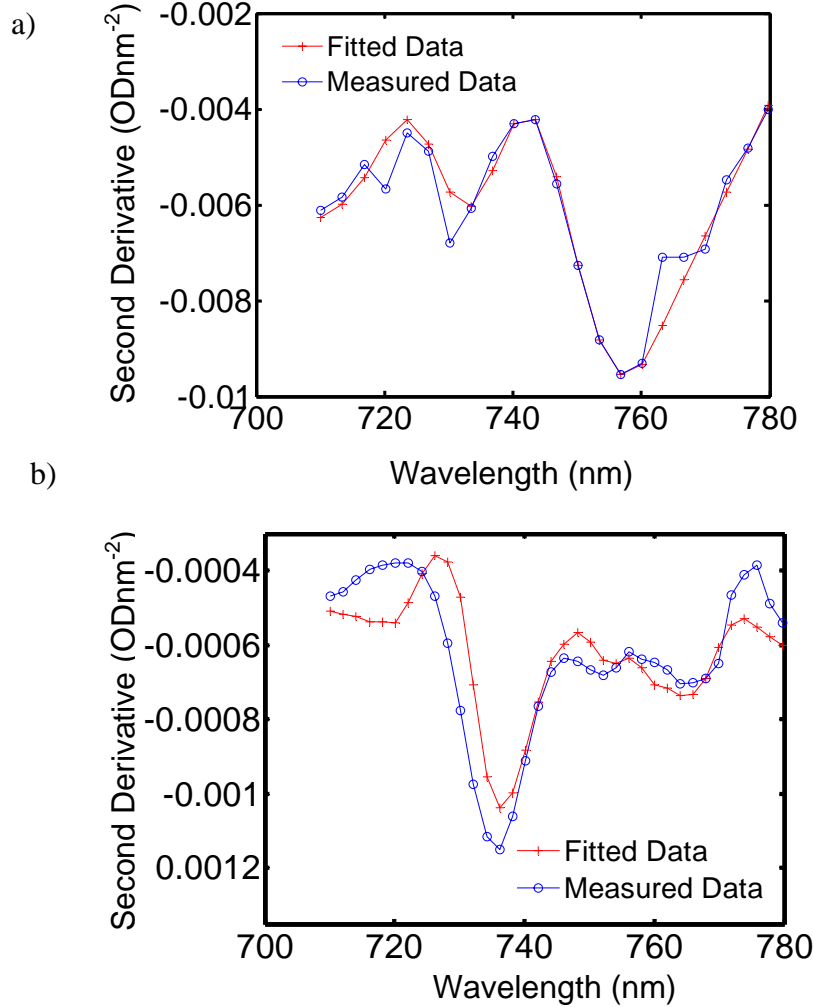


Figure 13 Comparison of measured second derivatives of the attenuation spectra and their corresponding fits to determine relative concentrations of Hb with respect to water. The line with blue circles indicates the measured data from the phantoms and red line with plus signs indicates its corresponding best fit. (a) is for a deoxygenated state with $[Hb] = 25 \mu M$ (26.7 μM) (b) is for an oxygenated state of $[Hb] = 1.3 \mu M$ (2.3 μM). Values in parentheses indicate concentrations measured by the ISS Oximeter. Values outside represent Hb concentrations determined from the second differential spectroscopy. Water content was calculated to be 97% in phantoms by volumetric measurements.

Figure 14 displays a comparison of normalized diffuse reflectance (using the 2nd normalization method) measured from a couple of phantoms and their best fits for hemoglobin derivative concentrations and reduced scattering coefficients. The oxygenation dependent spectral features are clearly seen. Figure 14(a) shows the typical spectral features for a deoxygenated state and Figure 14(b) for an oxygenated state. The optimization algorithm described in Section F.2 is used to calculate $[HbO]$, μ_s' (i.e., parameters c , d) and refine the water content that was assumed during the second differential spectroscopy. The $[Hb]$ information is used as a priori information to calculate the other parameters. The values determined from our algorithm and those measured by the ISS Oximeter are consistent, as listed in the legend of Figure 14.

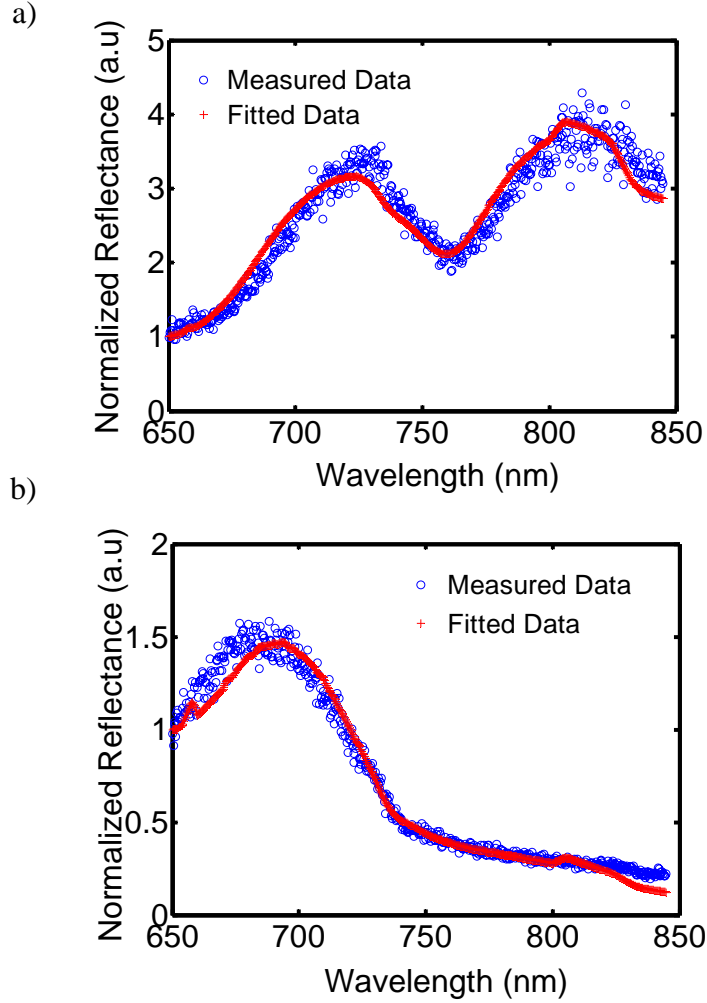


Figure 14 Normalized diffuse reflectance spectra. This is based on the 2nd normalization method: the reflectance values are normalized to one at $\lambda=600$ nm. (a) A spectrum for oxygen saturation of 96.6% with $[Hb]=1.3$ μM , $[HbO]=42.5$ μM , and $\mu_s'(750 \text{ nm})=6.2 \text{ cm}^{-1}$ (5.8 cm^{-1}). (b) A spectrum for oxygen saturation of 37.3% with $[Hb]=25$ μM , $[HbO]=15.0$ μM , and $\mu_s'(750 \text{ nm})=6.2 \text{ cm}^{-1}$ (5.8 cm^{-1}). Blue dots indicate the measured data from the phantoms and red curves indicate the best fits computed from the optimized hemoglobin derivative concentrations using our algorithm. Hemoglobin concentrations and μ_s' values measured by the ISS Oximeter are indicated in parentheses.

Figure 15 shows the least-squares fit to the μ_s' values, obtained from my algorithm, and those measured by the ISS Oximeter on the blood-intralipid phantom. As expected, the wavelength dependence of μ_s' in the NIR wavelength range is fairly smooth, weak, and possibly predictable. It is evident that the determined values of the reduced scattering coefficients lie within the error ranges of the ISS oximeter. The error bars are derived standard deviations from the ISS Oximeter measurements.

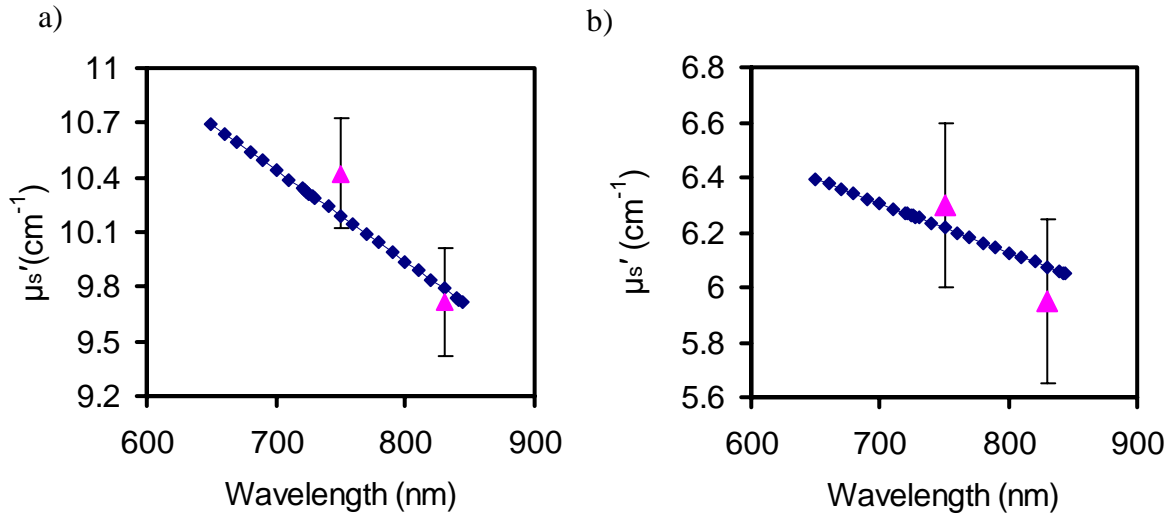


Figure 15 Broadband μ_s' spectra for two blood-intralipid phantoms. Triangles represent discrete μ_s' values measured by the ISS Oximeter, Diamonds are the best fits obtained from my algorithm. (a) Spectrum of μ_s' with $\mu_s'(750\text{nm})=10.1 \text{ cm}^{-1}$ (10.6 cm^{-1}) and $\mu_s'(830\text{nm})=9.9 \text{ cm}^{-1}$ (9.7 cm^{-1}). (b) Spectrum of μ_s' with $\mu_s'(750\text{nm})=6.2 \text{ cm}^{-1}$ (6.3 cm^{-1}) and $\mu_s'(830\text{nm})=6.1 \text{ cm}^{-1}$ (5.9 cm^{-1}). The error bars shown are the derived standard deviations from the ISS Oximeter measurements.

The advantage of using tissue-equivalent phantom data to validate the algorithms is that one can also gauge the extent to which the algorithm is model specific, e.g., one can test whether a favored algorithm performs equally well when applied to data generated using a different set absorption and reduced scattering coefficients. The analysis has been repeated for a range of concentrations of $[Hb]$ and $[HbO]$ as well as reduced scattering coefficients using a wide range of tissue like phantoms.

Results of research toward Aim 3 from PI Popa

Objective: to control the delivery of drugs using a novel implantable micropump (IDDS)

A. Introduction

The central idea of the IDDS is to utilize the well established principles of intravenous therapy (IV) to deliver controlled amounts a cancer drugs. Microelectromechanical (MEMS) technology has found useful application in many aspects of human life including bio-medical technology. MEMS have the advantage of using existing silicon fabrication technologies which can be integrated with CMOS devices while adding the functionality of mechanical systems. Because of their small size, MEMS can be implanted in the human body to monitor a variety of conditions, and to actively treat them. The systemic delivery of certain drugs e.g. chemotherapeutic drugs are know to have shortcomings such as toxicity, reduction in drug efficacy, and degradation of drug's therapeutic effects during transportation [44-46]. Yet, systemic administration of drugs remains the delivery method for most medications [45]. The motivation for using MEMS technology to create Implantable Drug Delivery Systems (IDDS) is to minimize the problems associated with the systemic delivery of certain drugs. This is achieved by 1) delivering precisely controlled, small amounts of medication (delivery rates up to 100 $\mu\text{l}/\text{min}$), and 2) targeting the drug to the localized, affected area in the body. The device described in this report, a micropump, aims to use these advantages to develop a centralized or localized implantable drug delivery device for chemotherapy by integrating a subcutaneous reservoir, an in-plane silicon pump and associated circuitry [19,25,39,53,54,66].

Micropumps play a key role in microfluidic circuits where nano or pico-liter volumes of fluid are delivered and controlled for applications to biotechnology, drug discovery and drug delivery. In general, diaphragm driven pumps have self-priming advantages compared to electrically driven pumps, and a variety of actuation principles, valve mechanisms and fabrication processes have been used to build diaphragms. Current pump designs consist of multiple layers, where each layer has a unique function, such as a diaphragm, valve, or actuator. However, multiple layer structures require expensive wafer alignment and bonding as well as externally assembled actuators.

From several discussions with physicians involved in treating cancerous tumors, it is evident that the addition of an implantable micropump would alleviate a lot of the discomfort suffered by patients using available treatments. Currently, most patients are administered cancer-fighting drugs through an external pump, which means that they must remain immobilized for extended periods of time. The benefits of a small, implantable delivery system will also include the ability to precisely control drug dosage over the many days required for treatment. The benefits of an IDDS are apparent in the case of cancer treatment, in particular prostate cancer. Such treatments often require continuous delivery of cancer drugs once a week. The delivery can take place over 24-48 hour period, after which there is no treatment for the rest of the week. Current delivery methods include intravenous pumping and drug injection. If the cancer is at the surface of

an organ, drugs delivered directly to that surface might work well, otherwise, and this is the case with most cancers, it is best to deliver the drug using the blood stream. In order to reduce the quantity of drug administered, it is possible to target arteries close to the affected organ, but there is always a risk for metastasis. Furthermore, if the cancer is hard to reach, the drug can be injected directly into the tumor, but this is less reliable and less effective than blood delivery.

During this project, we have prototyped a novel, monolithically fabricated micropump referred to as an in-plane micropump. This pump includes three major components: a diaphragm, an actuator, and a valve, all in a single layer. The pump is part of a packaged IDDS unit including a sub-cutaneous port reservoir, microfluidic interconnects, on-board power and control circuitry as shown in the diagram in Figure 1.

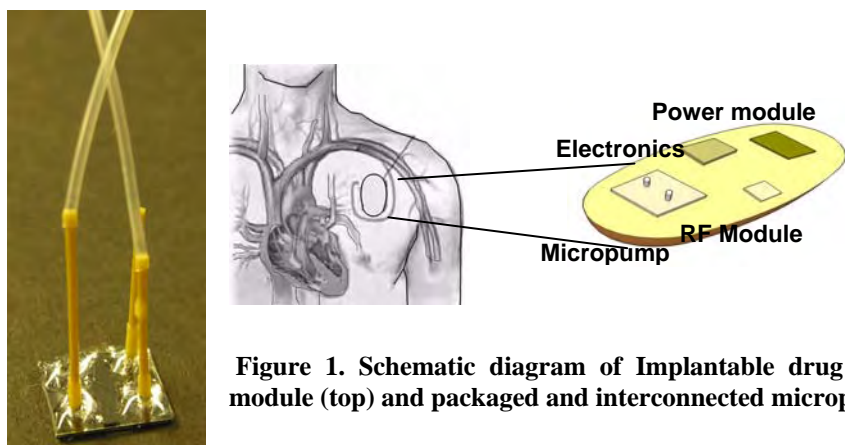


Figure 1. Schematic diagram of Implantable drug delivery system (IDDS) module (top) and packaged and interconnected micropump (left)

In the case of cancer treatment, conventional intravenous therapy relies on positioning the fluid bag to deliver the drug, as in “gravity drip” or infusion pumps to pump the drug into the circulatory system. These however limit patient mobility by confining them to a bed side infusion for several hours. The MEMS based IDDS aims at providing all the benefits of conventional IV therapy with a small implantable pump that has minimal impact on patient mobility. Research to meet the strict control required for dispensing therapeutic agents at specific intervals of time using micropump has been carried out since the early 1980’s. One of such pumps is that of Jan Smits designed to deliver insulin [16,17]. Other applications of pumps include the use of micropumps in drug delivery for cancer, chronic pain, spasticity, etc. Pumps may be classified as displacement-driven and dynamic pumps which include centrifugal, electro-hydro-dynamic and electro-osmotic delivery mechanisms [5,7,11-19,34,49,55,69,70]. Pumps operate by adding mechanical energy to the fluid. If the energy is added in periodic manner they are termed as displacement micropumps and if the energy is added continuously they are called dynamic pumps. In our case, we are developing a displacement micropump, based on an in-plane design and stacked die package.

A basic requirement of any micro-pump is the micro-actuation mechanism for precise fluid dispensation. The choice of the actuation method depends on several factors such as displacement stroke and force requirements, pulsing frequency, power requirements, etc. Micro-actuators are micro-devices that utilize any of several actuation mechanisms to

produce displacement or force. The general principle involved in the operation of MEMS based actuators is to convert energy from one form to the other and ultimately to produce positional change (deflection) or force. Examples of actuation mechanisms for micropump micro-actuators includes piezoelectric [13], magneto-static [47], thermo-magnetic [37,48], electrostatic [49], electro-thermal [50-52], etc., with electro-thermal micro-actuators being of special interest as a result of its inherent advantages such as low voltage requirements and high actuation forces. Some implantable micropumps have been used to deliver pain relief medication or insulin, and some are commercially available [5,11]. At present, the cost of an implantable insulin delivery system is still prohibitively high, while its long-time reliability is questionable [8]. Furthermore, the treatment benefits of an implantable insulin delivery system have not yet been demonstrated in clinical trials and might not exceed those of external pumps, stents, or slow release micro and nano-capsules [8,10].

We also studied the effect of the package on the performance of the IDDS during implantation. We first present the design, fabrication, and lumped parameter modeling of the unpackaged micropump. We then describe the packaging process and construct a full-fledged, electrothermal FEA model for the packaged micropump. Unfortunately, this is a coupled thermo-electrical model, with meshes that must accommodate very small features (for instance, the Chevron beams have 12 micron widths, or the 2 micron air-gap under the actuators), as well as much larger package components (for instance the handle die, 1cm x 1cm x 1mm). As a result, the simulation time for the full-fledged models takes is considerable (hours, even on a fast computer), and is not suitable to conducting designs of experiments to select optimal package geometry or materials. We are interested in reducing the complexity of the model for the actuator, micropump channels, valves, diaphragm, handle die, and the outer package. This is carried out by decoupling the model into two parts: a) the microactuator and close surroundings, and b) the MEMS die, top cap, package, and surrounding media. Part a) will contain meshed elements for the microstructure, and Part b) will contain meshed elements for the macrostructure. In addition, the detailed electrothermal model a) is approximated by a thermal model that accounts for Joule heating in a structure equivalent to the Chevron beam, and the heat removal rates through the substrate, the fluidic channel, and the top chip. Finally, the two models are coupled via corresponding boundary conditions and we can obtain both the temperature distribution in the package, and the Force/Displacement profile of the MEMS actuator. We show that this method is accurate enough to describe the thermal dissipation in the micropump package, and can be run fast enough to enable a parametric design of experiments. Finally, modifications to the package geometry and materials are made in order to allow a modest rise in temperature (less than 4 °C) on the outer package as will be required when the pump is implanted in the human body. This is achieved by employing a two tier micro-pump package structure consisting of an inner Kovar carrier and an outer Polybutylene terephthalate (PBT) carrier. Using only the Kovar carrier would have resulted in 69 °C outer package temperature. The carrier shape is yet to be optimized at this time.

B. Micropump Description and Fabrication

The electrothermal actuator for our micropump is fabricated using a 500 micron thick SOI (silicon on insulator) wafer. The key elements that constitute the device are voltage pads, V-shaped chevron beams and a center shaft connected to the diaphragm through lever mechanism for stroke amplification shown in Figure 2. It consists of six chevron beams on either side of the center shaft. The beams are 1200 μm in length with a cross sectional area of 12 μm x 100 μm with a rib angle of 5.7°. The pump diaphragm is 750 μm in length, 100 μm in height and 50 μm wide. It also consists of 2000 μm x 100 μm x 100 μm (length x width x height) fluidic channel along with a nozzle/diffuser arrangement for flow rectification. The dimensions are based upon detailed optimization studies [13-14, 24]. A picture of fabricated substrates and Level-0 packaged prototypes are shown in Figure 2.

In contrast to traditional peristaltic micropump designs, which use an out-of plane pumping diaphragm, the in-plane pump consists of the actuators, diaphragms, reservoir and I/O fluidic valves fabricated on a single layer. Joule heating of the V-beams and lever mechanism amplifies the stroke of the pump. The fluidic path is enclosed by anodic bonding of a PyrexTM glass to the pump die, and the overall fabricated mask layout is shown in Figure 3. The targeted adjustable pump rate is 1-100 $\mu\text{l}/\text{min}$, but exact design values for prostate cancer will be determined as an outcome of a study of the relationship between drug release rate, tumor oxygen levels and therapeutic outcome.

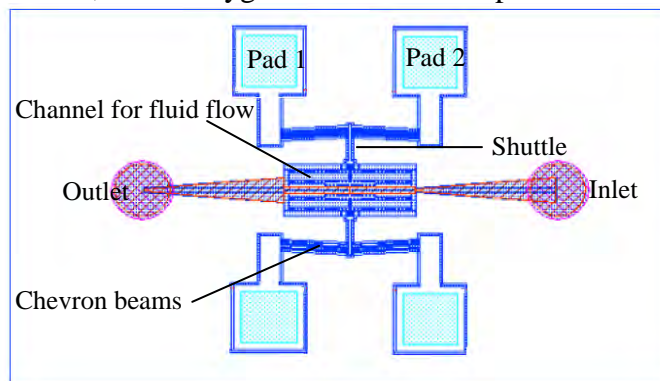


Figure 2: SOI MEMS layout of the in-plane pump

The actuator for our “in-plane” micropump design consists of electrothermal Chevron beams, micromachined on a SOI wafer using DRIE. Chevron beam actuators have been extensively studied in the past, including displacement and force analysis using FEA [55-58], as well as analytical or reduced order models [59-62], parametric design in terms of number of beams, beam size and bent-beam angle [63-66], etc. Accurate models for electrothermal actuators consider heat convection losses, conduction through the pads, as well as conduction through the air-gap between the actuator and the substrate [67]. Typical temperatures on the Chevron beams have also been verified experimentally, and found to be in the order of hundreds of degrees for 10-20 V inputs. In [68] the authors studied the effect of packaging an electro-thermal Chevron actuator by using a “top” glass cap die for protection. It is found that the beam temperature changes by up to 10% if an air gap beneath the glass cap die is increased from 2 to 3 μm . As a result, if the SOI

actuator die is attached and enclosed in a package, we expect that the Chevron beam temperature will also be affected.

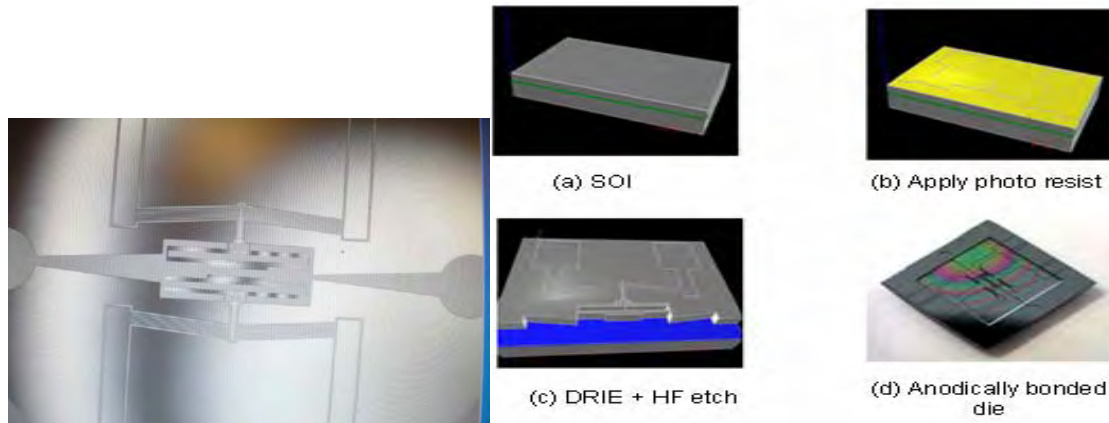


Figure 3: Fabricated SOI in-plane micropump, and a description of Fabrication and Level 0 Packaging steps

Other operating characteristics of the micropump are: 5 to 15 volt range for the pump, and a maximum flow rate of 100 μ l/min at 100Hz input. The new in-plane micropump reduces pump size and manufacturing complexity. The die level pump size is 2(W)x4(L)x1.5(T)mm³. The embedded actuator eliminates the need to externally assemble an actuator, and the monolithic structure reduces the need for high cost alignment and wafer level bonding. In this report we argue that this micropump can be manufactured at relatively low cost for applications such as implantable drug delivery systems. An exploded drawing of the pump assembly is shown in Figure 4.

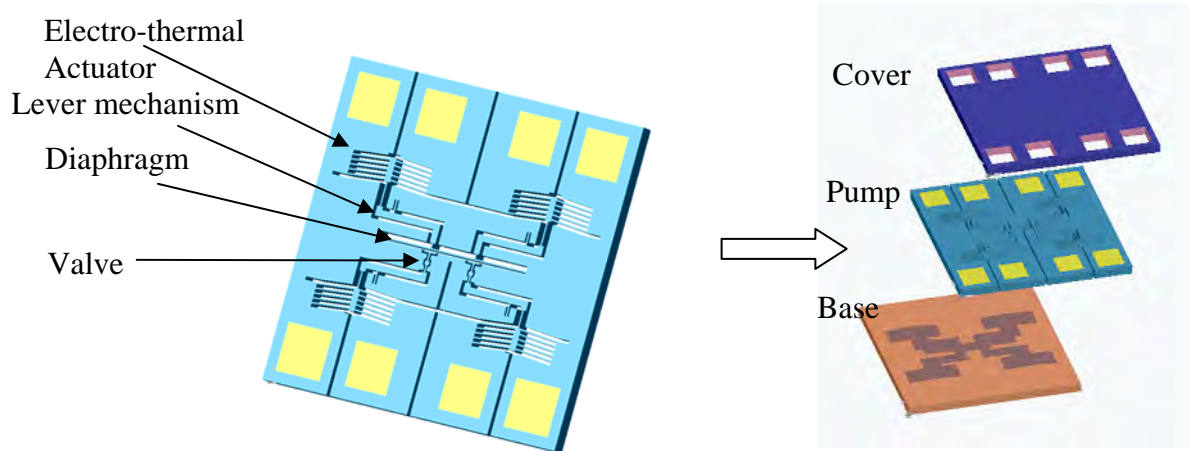


Figure 4: In-plane micropump. (a) An exploded view of a 3-layer design. (b) A micropump that has actuator, diaphragm and valves on a single die

The middle pump layer is stacked together with a top cover plate and a bottom base plate. A few micron step structure is engraved on both the cover and base plate to allow small gaps between the plates and moving parts of the pump layer. The cover plate has through-holes, which are used for electrical interconnections of the pump layer. The base plate has

through-holes for fluidic interconnection between the pump chamber and outside of the pump. Figure 5 shows microscope images of the actual fabricated samples.

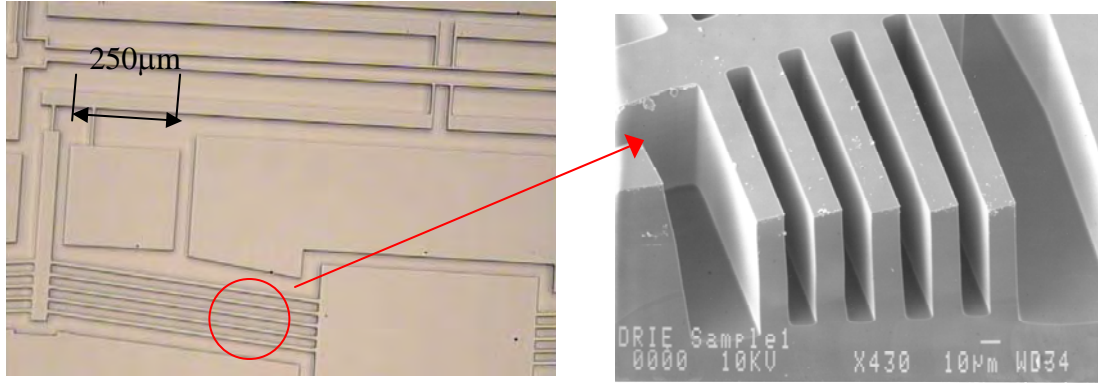


Figure 5: DRIE micromachined micropump structure. (a) In plane micropump. (b) SEM image of cross section of an electrothermal actuator.

The mechanical performance of the pump was simulated using both Finite Element Analysis (FEA) as well as a lumped model approximation. The results are shown in Figure 6. The simulation shows that the temperature at the center of the actuator is most hot region and it goes down quickly toward to the diaphragm.

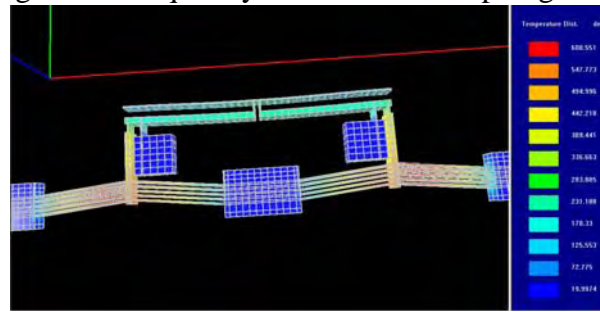


Figure 6: ANSYS® Simulation of electrothermal actuator in the micropump.

The simulation model was used to finalize the pump geometry prior to fabrication. Actual experiments were then performed to characterize the electrothermal actuators. The actuation mechanism consumes about 0.5W power, and it provides about 40μm stroke with an incorporated diaphragm. The full pump specifications are shown in Table 1.

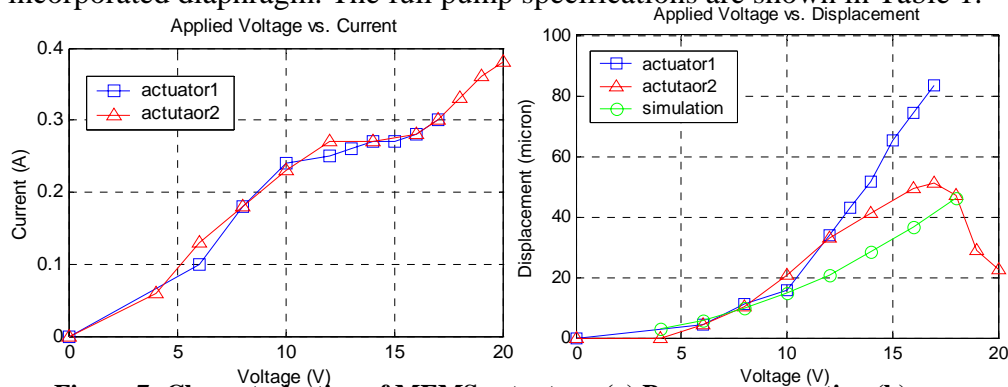


Figure 7: Characterization of MEMS actuators. (a) Power consumption (b) Displacement vs. Voltage

Parameter	Specification
Dimension	4mm×2mm×1.5
Pumping volume	3.6nL (chamber volume)
Compression ratio	3.5
Flow rate	~100 μ L/min
Back pressure	
Operating frequency	1~100Hz
Operating voltage	5~10V
Power consumption	0.5W

Table 1. Specifications of in-plane micropump.

Experiments were conducted to verify the displacement of the Chevron beam actuator and the pump diaphragm. For this analysis, we used a Veeco Wyko NT1100 DMEMS motion analyzer located at our Texas Microfactory™ Lab, shown in Figure 8. Dynamic analysis was carried out to quantify the displacement of the actuator as a function of time, phase, amplitude and frequency. The amplitude, phase, frequency of the input signal was varied together or in a sequence to describe the complete motion of the MEMS device. The dynamic response of the micropump provides information regarding maximum displacement and resonant frequency. Analysis was carried out with sinusoidal and square wave inputs. The voltage was varied from 8-24V and the frequency from 15-100Hz. For square wave, the duty cycle considered was 20%. The displacement of the chevron beam and the diaphragm was observed. The minimum and maximum displacement of the diaphragm was 2 μ m and 11 μ m respectively. The corresponding frequencies were 70Hz and 45Hz respectively. The cut-off frequency is 40Hz. The motion amplification through the cantilever transmission has been experimentally found to be approximately 5 times.

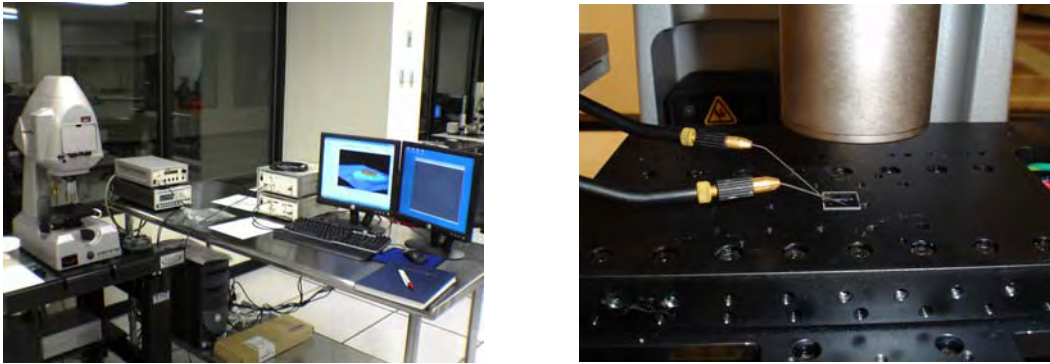


Figure 8: Veeco Wyko NT1100 Optical Profiling system (left), and a MEMS die being probed on this setup for motion characterization.

Based on the experimental measurements, the diaphragm pumping force was downgraded to 1.17 mN, based on which a flow rate of approximately 30 μ L/min is expected. Typical displacement plots of the diaphragm of the in-plane pump for square wave and sinusoidal input voltages are shown in Figure 9.

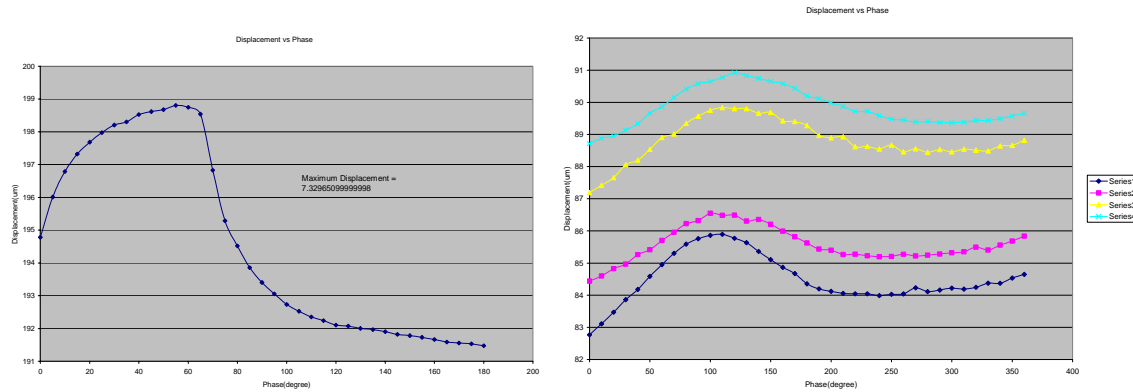


Figure 9: Displacement measurements of pump diaphragm for square wave input (left) and as a function of phase of sinusoidal input (right).

In addition to the MEMS die enclosed by Pyrex (Level 0 package), the pump must also be interconnected with electronics, power, and RF communication from inside the body. There are multiple levels of packaging, starting from Level 0 (SOI MEMS+Anodic Bonding of Pyrex), Level 1 (Enclosing the pump inside a carrier, and providing appropriate fluidic and electrical interconnects), and Level 2 (System level package by adding electronics, power, and a reservoir). During the period 2005-2006 we focused on modeling and simulation, in 2006-2007 we focused on Level 0 and 1 packaging and interconnects of the MEMS die, and in creating a basic Level 2 prototype for testing the micropump with cancer drugs, and in 2007-2008 we focused on testing the micropump and redesigning the Level 2 micropump package.

The reservoir, pump, catheter and associated circuitry will mimic the intravenous fluid bags and catheter. Conventional intravenous therapy relies on positioning the fluid bag to deliver the drug, as in “gravity drip” or expensive Infusion pumps to pump the drug into the circulatory system. These however limit patient mobility by confining them to a bed side infusion set up. The MEMS based IDDS aims to provide all the benefits of conventional IV therapy with a small implantable pump and provide mobility. When this micropump will be eventually tested on human subjects, a reservoir is also needed to ensure that drugs delivered through the implantable micropump can be replenished. Our reservoir is similar in design to the vascular access ports. These ports have been demonstrated to have good bio-stability and bio-compatibility. For this application, the reservoir should have smooth contours, hold at least 5 ml of the drug and be easily accessible for refilling. A subcutaneous position for the port-like reservoir is targeted for the IDDS, and Ti and Silicone materials will be used for biocompatibility (Fig 10).



Figure 10: Inch-size Titanium and Silicone port reservoirs, refillable through injection.

C. Micropump packaging

In general, MEMS packaging is more challenging than IC packaging. IC's in general do not have fragile, moving mechanical structures, they are not required to interface with the environment while at the same time, be protected from the environment, and they do not require micro-fluidic interconnection in tandem with electrical interconnections. In order to enhance the reliability of the micropump, the MEMS devices must be packaged appropriately. For the micro-pump, packaging provides electrical and fluidic interconnection paths; it provides a platform for component mounting and also protects the device from external damage caused by contamination, moisture and handling. It also ensures that adequate thermal solution is provided for heat removal. This is especially important for the IDDS because the surrounding cell temperature is expected to heat up no more than 4 °C. Equally important is ensuring hermetic packaging of the micro-pump to prevent drug leakage, and also, the choice of materials that ensure bio-compatibility while at the same time, ensures device reliability. There is a three level hierarchical structure to MEMS packaging, with each level expected to fulfill certain roles. These levels will be discussed later.

Packaging consists of anodic bonding of the micro-pump die and a cap chip, attachment of the bonded dies to a 1mm thick Kovar plate of dimensions 1500x1500 μm^2 via a 1mil thick thermal interface material (TIM). Wire bonding is done in order to provide electrical connections for the MEMS die. Lastly, the whole structure is sealed with Kovar metal cap. The schematic of the next packaging level for the die (Level 1) is shown in Figure 11.

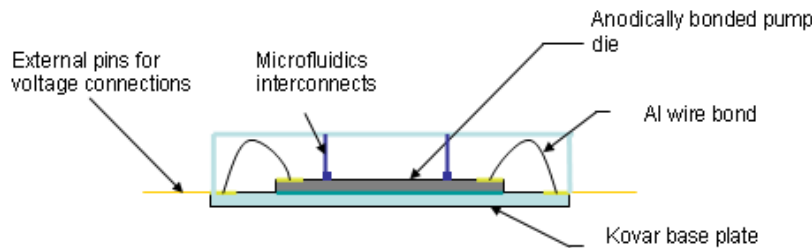


Figure 11: Schematic representation of the packaged pump die (Level 1 packaging).

C.1 Level 0 Micropump Packaging

The first level of micropump packaging is done using anodic bonding of the MEMS die with a Pyrex glass chip. This ensures that the fluidic pathways in the pump are created. The technique of bonding silicon and glass under the influence of temperature and voltage is known as anodic bonding. The formation of the bond involves the displacement of the sodium ions in glass by the applied field forming a depletion region at the surface. This highly reactive surface forms a strong chemical bond with the silicon. Anodic bonding requires very smooth and flat surfaces for bonding. It is also sensitive to contamination. The process conditions are temperature in the range of 200-500° C and voltage of 700-1.5kV. The bond strength is affected by voids or bubbles formed during the bonding process. It has been determined that the bonding temperature plays a critical role in bonding. Bonding time, potential and load contribute weakly to the bonding

strength but are key factors in influencing the speed of bond formation and the area bonded. The anodic bonding set up in our lab involves a hot plate, a pressure fixture and a high voltage source. Experiments were conducted to determine optimal process parameters, and an acceptable process window was found. The conditions for anodic bonding were temperature of 300-500 °C, and Voltage of 1-1.5 kV for 20-25 minutes, at low or no bonding force. The current flowing through the bonded region was monitored throughout the process and was found to be in the range of 9-20mA. The setup and bonded micropump dies are shown in Figure 12. In order to provide means for the interconnect through the Pyrex glass of 500 μm in thickness, holes were drilled in the Pyrex die prior to anodic bonding using diamond drill bits 650 μm in diameter to create holes in the range of 700-900 μm at a drill speed of 45,000 rpm. Experiments were conducted to determine acceptable micro drill process parameters and characterize the results. The drilling set up and resulting interconnect holes are shown in Figure 13.

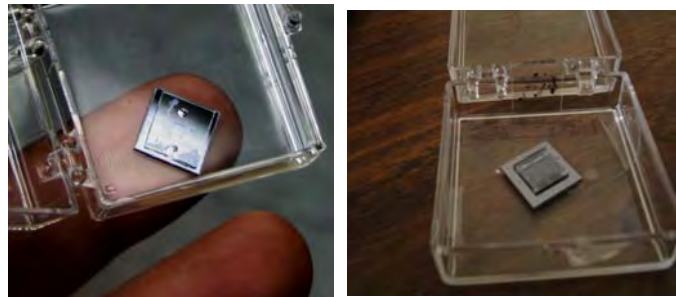


Figure 12: Anodic bonded samples (center, right), to form the pumping chamber between SOI and Pyrex dies.

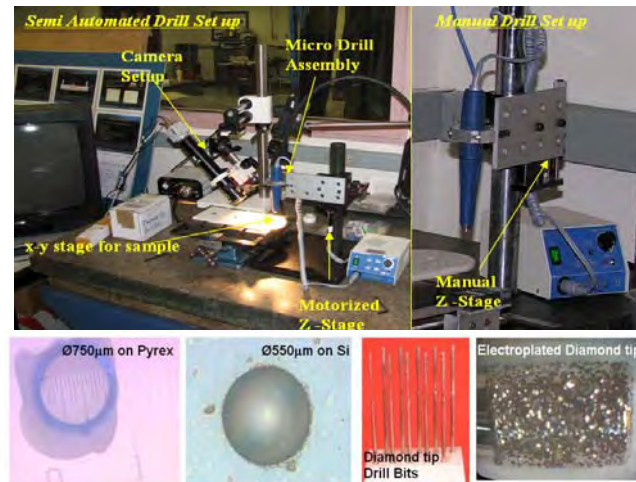


Figure 13: Pyrex micro drilling station and optical measurement of interconnect holes using a Veeco NT1100 surface profiler

Finally, the fluidic path inside the pump must be contained inside the MEMS device. The SOI MEMS contains 2 μm leak paths below and above the moving diaphragm in order to actuate, and therefore, it is necessary to contain the fluid flow using a compliant polymeric membrane implemented in the shape of a tube. In order to achieve this, it was proposed that a tube made of Parylene should be embedded in the channel connecting the inlet and outlet of the micropump. The Parylene tube would be in contact with the

diaphragm of the pump enabling the pumping of the fluid in the channel contained within the tube. The schematic drawing of the Parylene tube embedded in-plane micropump is as shown in Figure 14.

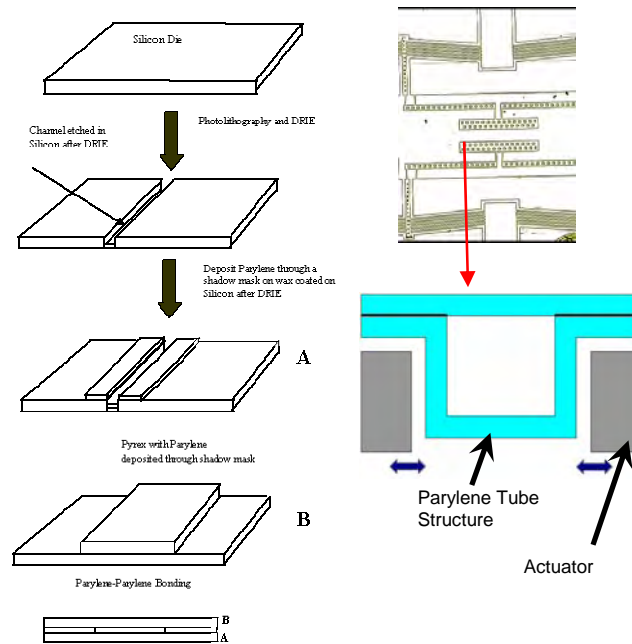


Figure 14: Schematic cross section of a Parylene tube inside the pumping chamber, and fabrication process.

The process of forming the Parylene-Parylene bond is followed by dissolving the molding wax in Toluene to form the tube structure on the Pyrex. This is then aligned and anodically bonded to the SOI micropump die.

C.2 Level 1 Micropump Packaging

For obtaining a package similar to the diagram in Figure 11, fluidic and electrical interconnects must be fabricated. Fluidic interconnects out of the pumping plane are formed by using PEEK or glass capillary tubes with Silicone tubing. These are bonded to the Pyrex using a fast curing epoxy as shown in Figure 15. In addition, the die stack must be placed inside a carrier package. Because the actuation principle we use is based on a thermal MEMS drive, it is important to study the effects of heat dissipation in order to design the thermal mass of the package and ensure that during device implantation tissues are not exposed to more than a few °C temperature increases.



Figure 15: Fluidic interconnects on the anodic bonded micropump die

We carried out Level 1 Package thermal analysis using in-depth numerical analysis. This was performed in order to determine the impact of each variable (air gap, voltage etc) on the maximum device temperature. Analysis was performed using ANSYS®. In order to ensure package hermetic sealing and thus prevent medication leakage to the body system, brazing technology is used to attach the carrier and the lid.

C.3 Level 2 Micropump Packaging

This level of packaging contains the micropump electronic circuitry for logic, driving, RF communication and power.

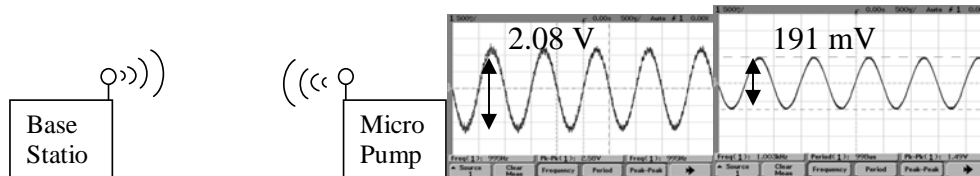


Figure 16: (a) Telemetry set up (b) transmitted and (c) received signal from the telemetry test setup placed 5m apart. The transmitted signal is a 1.2 mV_{p-p} amplified by a factor of 2000 and received signal is 191 mV. The modulated signal is a 1 KHz sine wave with a 433 MHz carrier.

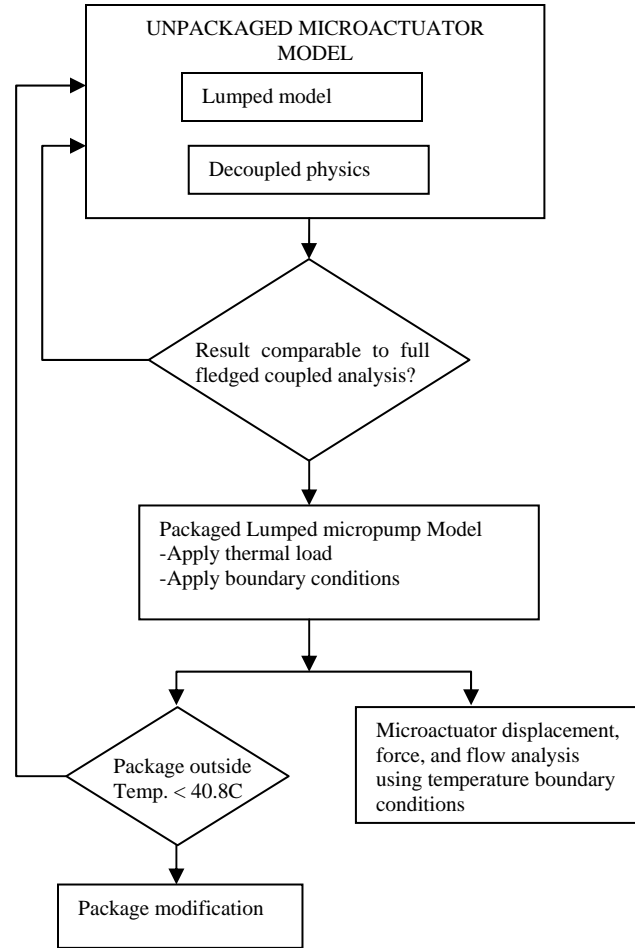
A telemetry module has been set up to ensure a wireless link from the micropump to a base station. The telemetry module consists of a transmitter unit and a receiver unit. The transmitter includes operational amplifiers, amplifier circuit, a miniature antenna and a transmitter chip. The receiver has a receiver chip and signal conditioning circuitry. The antenna chosen is a Copper solenoid of 24 turns. The antenna is soldered on a small printed circuit board with the transmitter chip and lumped elements with operating frequency of 433 MHz. The range of operation is sufficient for the proposed application since the base station will be close to the patient when the physician monitors and programs the implanted unit. Fig. 13 shows the signal received from a transmitter-receiver separated by a distance of 5 m. A 1 KHz sine wave was used to modulate a carrier of 433 MHz. It demonstrated clear communication between the transmitter and receiver. The transmitted signal is 1.2 mV_{p-p} amplified by a factor of 2000. The received signal is filtered by a bandpass filter, 300 Hz – 10 KHz, to reduce noise, especially 60-Hz power line signals and interference from other wireless instruments. The purpose of this demonstration is to show feasibility of telemetry, hence the size of the circuit board has

not been optimized. In the future, we intend to integrate the telemetry and microfluidic devices to deliver a completely implantable drug delivery mechanism.

Several other technical challenges must be investigated in the future. These include power management, size considerations, and control circuit integration. Without taking into account the power required by the RF unit, the estimated power consumption for the target 100 $\mu\text{l}/\text{min}$ delivery rate is in the range of 100-500 mW. This figure is estimated based on the power consumption of the micropump necessary to generate required diaphragm displacements. As a result, commercially available miniature lithium-ion batteries would discharge in less than 48 hours of operation. Therefore, a power management system employing recharging of the power source is also necessary in the IDDS. One possibility is recharging from outside of the body using through-skin electrical interconnects. A much better alternative would be wireless power transmission using RF coils.

D. Methodology for Package-Level Characterization of Micropump

Analytical solutions to complex thermal and structural problems are often lacking, making numerical approach to solving these problems very attractive. In our case, a multi-physics analysis of the packaged micropump should include thermal, structural and fluidic components. The numerical solution approach to solving near exact or detailed physical models at the package or system level, even when using commercial numerical codes such as ANSYS®, is difficult, requiring large meshes, coupled solvers, and a long processing time, even on very fast computers. As a result, such detailed models cannot be used to tweak design parameters, as would be required during a design of experiments optimization. In this paper, we reduce the model complexity via lumped or compact modeling, model symmetry, and decoupling of physics during the analysis of the packaged micropump. In particular, we want to decouple the intricate details present in a “microscale” model with the coarser meshes needed for a “macroscale” model. A flow chart of the methodology used in this work is presented below, while the methodology is described fully later in this section. We formally verify the validity of the electro-thermal-structural modeling results, and use the reduced order models to also estimate the expected flow of the micropump in both packaged and unpackaged states. As a result of this analysis, the reduced order models run much faster (minutes, rather than hours), while being accurate within 10% of their full-fledged models. The impact of packaging on the expected temperature and flow can be quickly assessed, as can package design changes. Using the result, we propose a modified package that satisfies implantation requirements for IDDS.



Schematic representation of used methodology for micropump thermal, displacement, and flow characterization.

D.1 Description and Use of Models

From an electro-thermo-structural-flow standpoint, we describe here several models as follows:

- **micro-model:** this model consists of detailed microactuator model with the rest of the device and handle layers, a top cap chip above the actuator, and 2 μm air gap layers beneath and above the microactuator. This is a thermo-structural model.
- **complete model:** this model consists of detailed microactuator model with diaphragm, handle layer, top cap chip, air gap layers below and above the microactuator, Kovar based carrier, and lid. This is a thermo-structural model.
- **macro-model:** this model consists of a simplified approximate geometry of the microactuator with the rest of the device and handle layers, Kovar carrier with lid, a top cap chip above the microactuator, and 2 μm air gap layers beneath and above the microactuator. This is a thermal model.

- **implanted macro-model:** this model is the same as the previous one, only it also contains a model of the surrounding human tissue when the device is implanted. This is a thermal model.
- **lumped flow model:** this model is an approximation of the pumping mechanism in order to estimate the fluid flow generated by the pump. This is a structural-flow model.

In order to validate these models, and use them during design packaging and pump flow estimation, we followed the following steps:

Step 1: Obtain a purely thermal model of the microactuator

We proceed with the analysis by performing electro-thermal analysis of the micropump's microactuator. This consists of the following steps:

- Simplify micro-actuator model by collapsing chevron beams into a lumped geometry with same resistance as the overall resistance of the detailed microactuator model.
- Simplify model physics by applying heat generation (or heat flux) on actuator beam instead of voltage, thereby decoupling the physics.
- Compare thermal result with full fledged coupled electro-thermal and determine error.
- Repeat 1-4 using different boundary conditions (BC) combinations to ensure that method yields consistently accurate results.

During this step, we eliminate the need for electro-thermal analysis on a detailed micro-model, by replacing it with a purely thermal load via Joule heating, and a simplified geometry of the micropump.

Step 2: Create a detailed, complete model of the packaged micropump with thermal load and boundary conditions only.

Now that we have eliminated the need for electrical boundary conditions, we construct a detailed thermal and structural model of the packaged micropump, and we use it as a benchmark to compare the accuracy of further approximations, the model complexity reduction, and the computational time savings.

Step 3: Create an approximate macro-model of the packaged micropump and validate against the model in Step 2.

To create a reasonable reduced order model of the packaged lumped model microactuator, we use the heat input of the micromodel and apply them to a macromodel using the following boundary conditions:

- Load: heat generation or heat flux.
- Boundary conditions:
 - Convective heat transfer coefficient of 25W/mK on exposed surfaces; and micropump diaphragm surface is maintained at 36.8°C due to fluid flow.
 - Convective heat transfer coefficient of 25W/mK on exposed surfaces, and we ignore heat losses through the fluid.

The second boundary condition represents the case in which heat loss is primarily due to diffusion via conduction into the package and convection to the ambient. We want to verify if heat extraction due to the fluid flow of the micropump is small enough and can be neglected. At this point, the package is assumed to have heat convection losses, and is not yet implanted inside the body.

Step 4: Create an approximate implanted macro-model

We now change the convection boundary conditions of the macromodel by “implanting” the micropump, e.g. surrounding it with an outer layer that simulates the body. This layer will have similar thermal conduction as water (the human body is composed of 90% water), and apply temperature boundary conditions on the outside layer consistent to that of a constant temperature at 36°C.

Step 5: Use the detailed micro-model with appropriate boundary conditions to calculate for actuator displacement

On a micro-model consisting of detailed actuator, wafer handle, and top cap chip we use the following assumptions:

- Load: heat generation or heat flux
- Boundary conditions:
 - Average temperatures on the handle wafer and top cap chip obtained from the macromodel in Step 4.

We then compare result of actuator displacement with full fledged thermo-mechanical model to verify accuracy and determine pushing force of the thermal actuator for different input voltages applied to the microactuator.

Step 6: Create a lumped-parameter approximation of the flow model for an unpackaged micropump.

This model will calculate the flow rate generated by the micropump given peristaltic forces applied on the pump chamber diaphragm.

Step 7: Compare the packaged and unpackaged microactuator force on the pump diaphragm.

Here we compare the pumping force of micro-model in Step 5, with the force obtained with the same, but unpackaged micro-model. We then use the estimate in pumping force to calculate the packaged pump flow rate using the model in Step 6.

Step 8: Propose package modifications using macro-model in Step 4 in order to achieve a target implanted outer temperature.

Using the model in Step 4, we perform necessary modifications to package carrier to ensure that the outside temperature on the carrier does not exceed 40.8°C, and can thus be safe to use inside the human body.

E. Thermal and Flow Analysis of the Micropump

In this section, we present the results of thermal, mechanical and fluidic modeling of the package micropump. In order to reduce the complexity of the analysis and the computational time, simplified models were used. However, in reducing the complexity, we needed to ensure that we are able to estimate the error introduced by such simplification, that the error is consistent, predictable, and within reasonable limits. The model and analysis simplifications consist of:

1) **Device geometry simplification.** 6 pairs of chevron beams on either sides of the shuttle are represented by a single structural beam with equivalent electrical resistance. Since the chevron beam dimensions are small compared with other dimensions on the device, the device electrical resistance may be approximated by that of the beams. The thermal analysis is then carried out on the simplified device model. Results using both the coupled electro-thermal analysis and a pure thermal approach are presented for the simplified design. The actual design and the modified design are shown in Figure 17. This modification is useful for the thermal analysis of the micro-pump actuator but cannot be used for mechanical analysis because of geometry and geometrical constraints between the actual and simplified models.

2) **Further simplification by decoupling the physics.** We decouple the electro-thermal model into a single field (thermal) field problem by applying either volumetric heat generation or heat flux on the actuator beams instead of applying voltage on the pads. It is essential that the overall electrical resistance of the two models (detailed and lumped micro-actuators) be similar. A simplifying assumption is that the resistance (more appropriately, the resistivity) of the beams are temperature independent. With the applied voltage and resistance known, the joule heating on the actuator beams can be determined from:

$$P = \frac{V^2}{R}, R = \rho \frac{L}{A},$$

where R is the electrical Resistance (Ω), V is the applied voltage (V), P is the dissipated power (W), ρ is the resistivity of doped silicon (Ω/m), L is the total length of the chevron beams, and A the equivalent cross-sectional area of all beams.

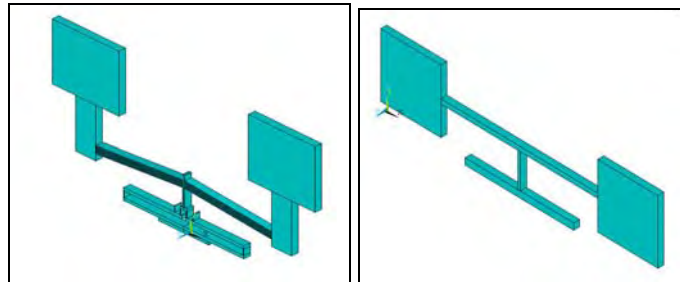


Figure 17: (a) Detailed (actual) microactuator model with six chevron beams on either sides of the shuttle and (b) simplified device models with collapsed beam representing the chevron beams.

E.1 Lumped and Detailed Thermal Analysis of Micro-Actuator

We first compared the results of coupled field electrothermal analysis of the detailed microactuator with that of thermal analysis of the detailed microactuator to ensure that the electrothermal model with applied voltage as input power is equivalent to the thermal model with applied heat generation (or heat flux) as the input power. The results of the steady state analysis at different power level indicate less than 1% error between both models as shown in Figure 18. The element Solid98 and Solid87 elements were used for the coupled field electrothermal and single field thermal problems. Each model comprised of 12,574 elements, and the computational time for solving the thermal model is about half of that for the coupled field model. For the coupled field problem, the load was applied as voltage input (loading scenarios of 4, 6, 8, 10 V were considered) while for the case of single field thermal, the load was volumetric heat generation by the microactuator beams. The value of the heat generation was obtained from the voltage input, the resistance of the actuator, and the volume of the microactuator beams. The boundary condition for both cases is convective heat transfer of 25 W/m²K.

Next, we compared the results of electrothermal analysis of the detailed microactuator model shown in Figure 17a with that of thermal analysis of lumped microactuator model shown in Figure 17b to determine if we can replace the full fledged electrothermal analysis of the detailed microactuator with thermal analysis of simplified microactuator model. In this case, the error level was less than 5% as shown in Figure 19.

The load and boundary conditions (B.C.) for these analyses are:

Load: 4, 6, 8, 10, 12, and 14 V

B. C.: 36.8°C on the pad surfaces, and convective heat transfer coefficient of 25 W/mK on exposed surfaces.

The key material properties used in this work are given in Table 2. By using this approach, the simulation time was reduced from over 8 minutes to less than 25seconds (~1/200th reduction in computation time).

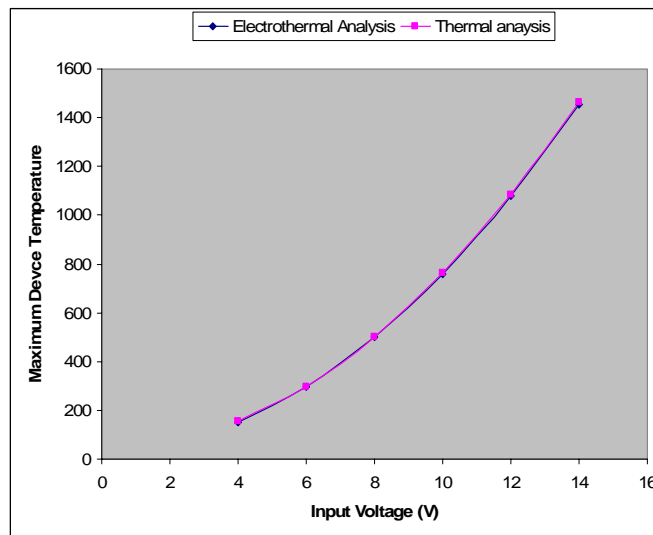


Figure 18: Electrothermal analysis of microactuator: detailed model Vs. lumped model.

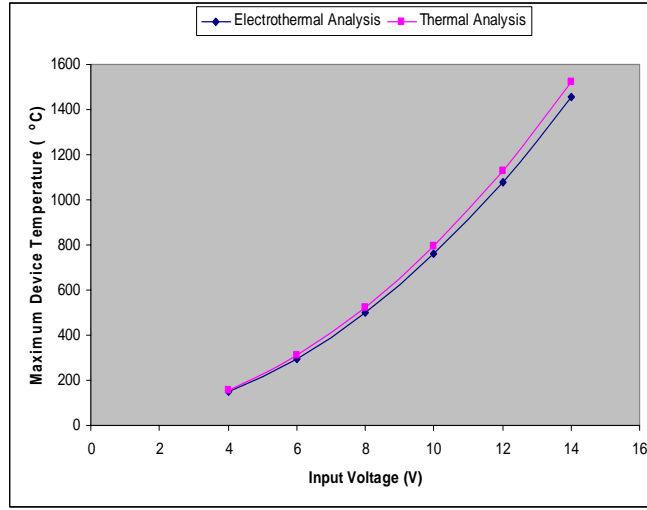


Figure 19: Thermal analysis of microactuator: electrothermal analysis Vs. thermal analysis.

Table 2: Material properties values used for micropump models.

Entity	Density (J/kg ³)	Specific Heat (J/KgC)	Thermal Cond. (W/mC)	ρ (Ω -m)
Device Layer	2300	720	150	1.1E-04
Oxide Layer	2200	700	1.4	5.05E15
Air	0.1239	1006	0.024	2.0E13
Handle Layer	2300	720	150	2.3E-5
Glass	2230	753	110	400E6
Kovar	8360	439	17.3	0.49E-6

E.2 Thermal Analysis of Packaged Micropump

From the results of section E.1, we gained confidence that by reducing the problem to single field thermal analysis from a coupled field electrothermal analysis, we do not lose much accuracy. In this section, we describe the steady-state analysis of the packaged micropump consisting of lumped microactuator model, the micropump device layer, the top cap chip, Kovar based carrier and lid. The approach here is similar to that of section 5.1 with the problem reduced to single physics (thermal) analysis of a packaged lumped microactuator. The thermal load was applied as volumetric heat generation. We will discuss results of the instance of the following two boundary conditions: convective heat transfer coefficient of $25\text{W/m}^2\text{K}$ on exposed surfaces; and micro-pump diaphragm surface is maintained at 36.8°C due to fluid flow. Simulation results show that boundary condition 2 represents an extreme case in which heat loss is primarily due to diffusion via

conduction into the package and convection to the ambient. We further note that the effect of fluid flow across the pump's diaphragm at expected pump working voltage is about ~10% reduction in the peak temperature of the micropump as shown in Figure 20.

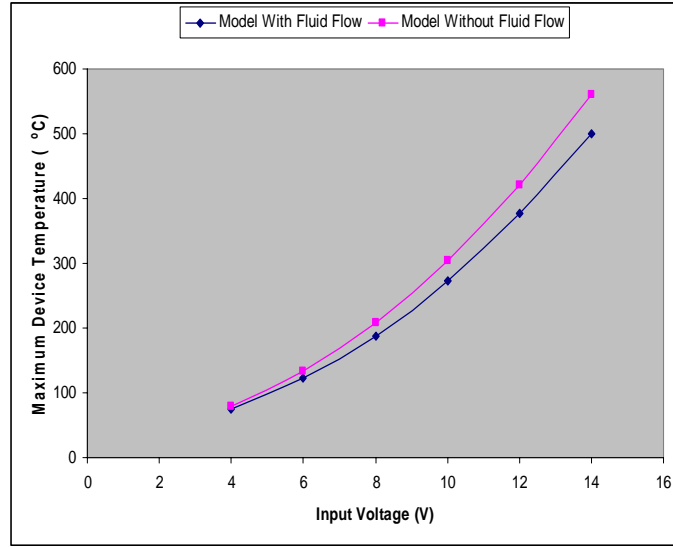


Figure 20: Thermal analysis of micropump: model with fluid flow Vs. model without fluid flow.

We also notice the effect of packaging on the maximum device temperature for corresponding power input levels. For instance, at loading condition corresponding to power input level of 4V, the maximum device temperature is reduced from 158°C (for the unpackaged microactuator shown in Figure 10) to 79.6°C (for the packaged case shown in Figure 12). We further notice the effect of increased thickness of the air gap layer between the device and the top cap chip. The air gap layer is modeled as a thin conduction layer with almost zero modulus. By increasing the air gap thickness, the thermal resistance offered by air gap increases therefore increasing the maximum device temperature. By increasing the air gap thickness from 2 to 5 μm , the device temperature increased by up to 17% over our input power range of 4 to 14V as illustrated in Figure 21.

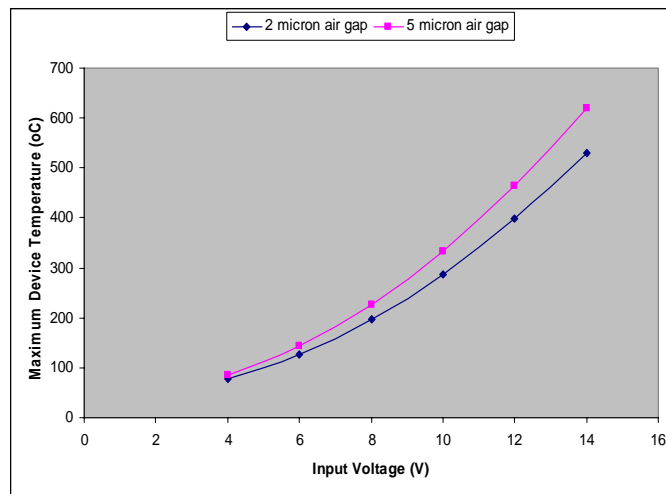


Figure 21: Effect of air gap on device temperature

We can conclude that:

- 1) It is reasonable to ignore heat losses due to the fluid flow in the micropump package. This leads to a simpler macro-model.
- 2) The air gap between the cap chip and the electrothermal actuator greatly influences the actuator temperature. In a similar work, increasing the air gap between the device and the top cap chip from 2 μm to 3 μm resulted in 10% increase in device temperature [68].

E.3 Actuator Displacement and Force

It is computationally intensive to solve the coupled field (thermal-structural) problem for the complete package. The micro-actuator deflection analysis was solved using sequential coupled method whereby the result of the thermal problem is used as the input for the structural problem to obtain the microactuator deflection. A simplifying assumption was that the structural problem does not significantly impact the thermal state of the device. This problem was solved using heat flux as the thermal load and the results obtained were compared with that of using volumetric heat generation as the thermal load. The temperature over each of the pump's surrounding structures (top cap chip and handle layer) from section E.2 were used as thermal boundary conditions for the thermal-structural analysis of a model consisting of detailed microactuator structure, device layer, air gap layers, top cap chip, and handle layer to determine the microactuator displacement. The structural problem is then solved via sequential coupled analysis in which the thermal result from previous step served as input for the structural analysis.

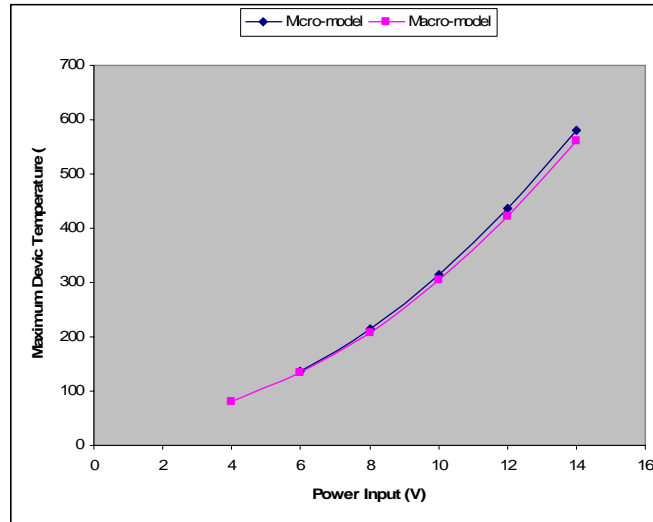


Figure 22: Device maximum temperature: macro-model Vs. micro-model.

Using heat flux value corresponding to 4, 6, 8, 10, 12, and 14V power input, convective heat transfer coefficient, h of $25\text{W/m}^2\text{C}$ on all surfaces, and applying the average temperature of both the substrate and the glass cover as boundary conditions, the thermal problem was simulated. The solution obtained from this step served as the input for the structural problem. The results obtained were compared with those obtained in section 5.2 (packaged lumped microactuator model without fluid flow). The difference in the

results is less than 7% as shown in Figure 22. At input power level of 8V, the maximum actuator deflection was 10.1 μm as shown in Figure 23.

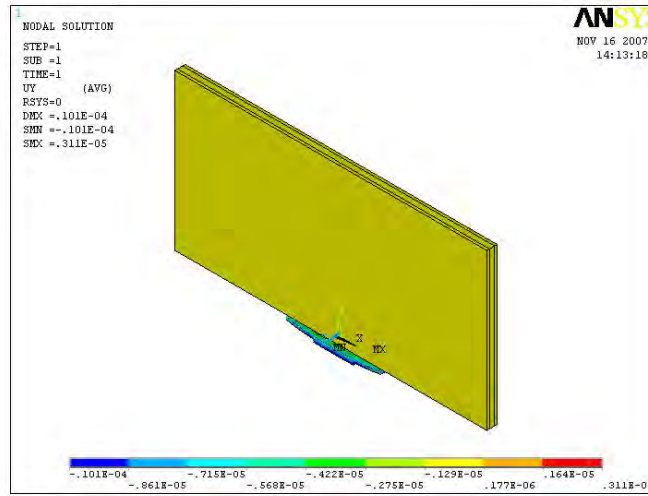


Figure 23. Micro-actuator displacement at 8V input.

The displacement values obtained for the packaged micropump are shown in Table 4. In this table, X_i is actuator displacement using temperature boundary conditions on the substrate and the cap chip, while X_f is actuator displacement using temperature boundary conditions on the substrate and the cap chip, and also, heat flux corresponding to 4, 6, 8, 10, 12, and 14V on actuator beams. T_i and T_f are the maximum device temperatures at X_i and X_f respectively. The difference between X_f and X_i is the net actuator displacement. The displacement and temperature values for the unpackaged microactuator are presented in Table 4. For a given voltage value, packaging results in reduced device temperature and displacement.

Table 3: Microactuator displacement for packaged micropump.

Voltage V	X_i (μm)	X_f (μm)	T_i ($^{\circ}\text{C}$)	T_f ($^{\circ}\text{C}$)
4	1.96	3.3	51.21	82.6
6	3.08	6.1	69.2	139.9
8	4.65	10.1	94.5	220.1
10	6.67	15.1	126.79	323.2
12	9.14	21.4	166.41	449.2
14	12.1	28.7	213.5	598.3

Table 4: Microactuator displacement for unpackaged micropump.

Voltage V	Displacement (μm)	Temperature ($^{\circ}\text{C}$)
4	7.52	140.7
6	16.3	285.3
8	28.6	487.7
10	44.4	747.9

The actuation force may be determined experimentally by measuring the deflection of a cantilever beam of known stiffness. Using simulation, we determined the actuation force by estimating the counterbalancing force F needed to establish equilibrium (zero displacement) of the device as shown in Figure 24. This force is a function of the thermal strain caused by current flow in the actuator beams. This force is obtained by calculating the stiffness of the microactuator before the incidence of buckling takes place (within the elastic range) from the force and displacement values. The force/displacement values obtained for the case of 8 V input power are given in Tables 5 and 6 for both the packaged and unpackaged microactuators.

The stiffness values (slope of the force/displacement curve shown in Figures 25 and 26) for the packaged and unpackaged cases are 925.4 N/m and 701.8 N/m respectively while the actuation force (y-axis intercept of the force/displacement curve) for the packaged and unpackaged cases are 9.3 mN and 20.1 mN respectively. The difference in stiffness values for the two cases is due to the reduced device temperature as a result of packaging.

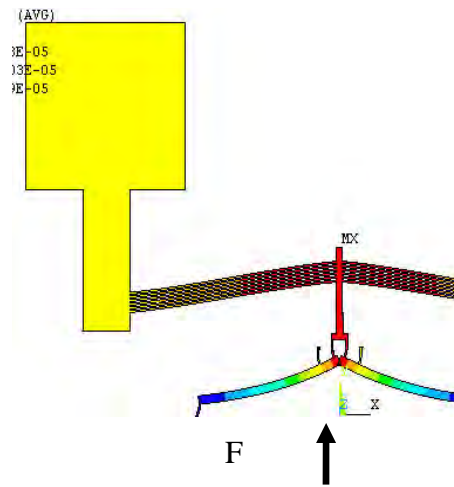


Figure 24: Counterbalancing force F needed to establish equilibrium (zero displacement) of the micropump.

Table 5: Microactuator force/displacement values at 8 V for packaged device.

Force (N)	Displacement (m)
0	1.01E-05
0.001875	8.04E-06
0.00375	6.00E-06
0.005625	3.97E-06
0.00675	2.83E-06

Table 6: Microactuator force/displacement values at 8 V for unpackaged device.

Force (N)	Displacement (m)
0	2.86E-05
0.001875	2.59E-05
0.00375	2.32E-05
0.005625	2.05E-05
0.0075	1.78E-05
0.01125	1.26E-05

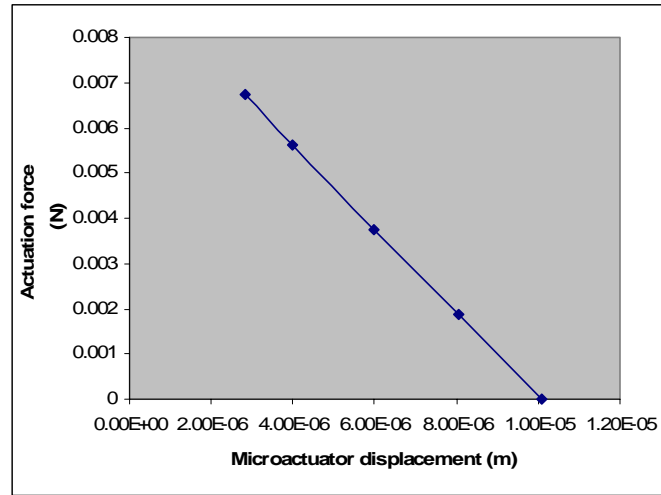


Figure 25: Force/displacement plot for packaged device.

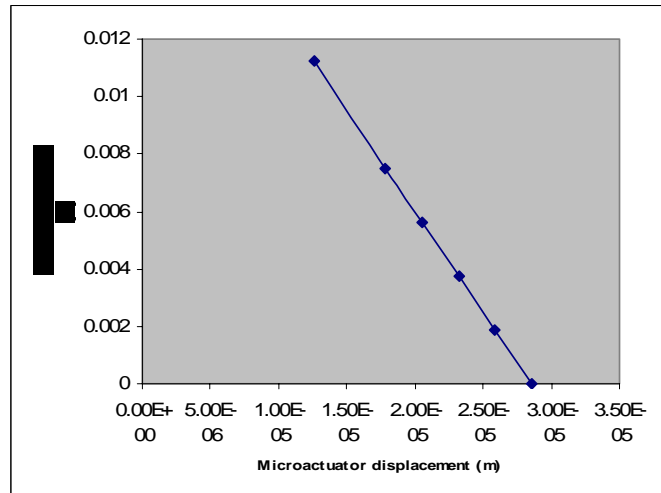


Figure 26: Force/displacement plot for unpackaged device.

E.4 Fluid Flow

In order to guide in the micropump design parameters, we used Finite Element Analysis. Due to limitations of FEA to model electrothermal, displacement and flow effects simultaneously, we also developed a lumped parameter dynamic model to calculate the flow as shown in Fig. 27. Motion obtained by flexing the diaphragm is simplified to the motion of a piston of mass $m = 3 \mu\text{g}$. Based on the finite element model of the actuator and diaphragm the stiffness is $k = 200 \text{ N/m}$ and the actuator force $F = 6 \text{ mN}$ for a voltage input of 15 V was fed into the lumped parameter model.

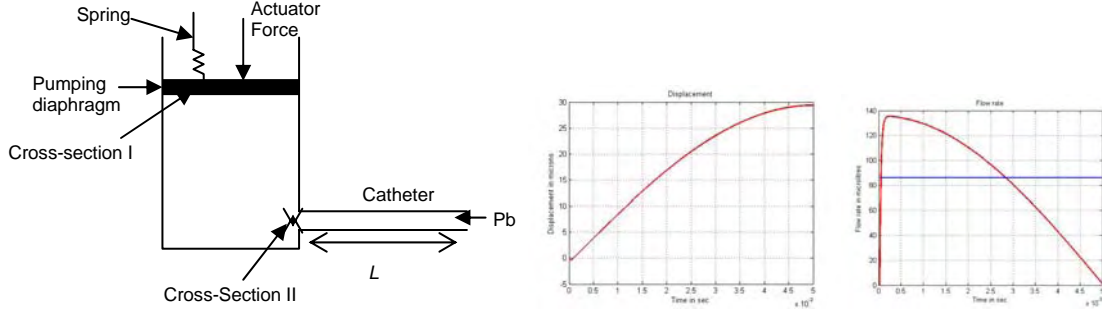


Figure 27: Lumped parameter model used to estimate flow rate of the micropump (left), pump diaphragm displacement and flow plots for one pumping stroke (center and right)

By writing the dynamic equations of motion and the continuity and Bernoulli flow equations we obtain:

$$\begin{aligned}
 m\ddot{x}_1 + b\dot{x}_1 + kx_1 + p_1 A_1 &= F, \\
 A_1 \dot{x}_1 &= A_2 \dot{x}_2, \\
 p_2 + \frac{\rho \dot{x}_2^2}{2} &= p_1 + \frac{\rho \dot{x}_1^2}{2},
 \end{aligned} \tag{1}$$

in which x_1 is displacement of piston, p_1 is pressure below the piston, A_1 is cross-section of the piston equal to 1.44 mm^2 , x_2 is outlet flow velocity, A_2 cross-section of outlet equal to 0.78 mm^2 , ρ is the density of the liquid, b is the diaphragm damping factor. In our simulations, b was chosen to critically damp the system, e.g. $b = 2\sqrt{km}$. The outlet of the pump chamber is connected to a catheter of length L equal to 10 cm and diameter D equal to $500 \text{ }\mu\text{m}$ that connects the pump to the vein. Based on physiological data we assume that the back pressure at the end of the catheter is $P_b = 8 \text{ mmHg}$, therefore a pressure boundary condition for our model is $p_2 = p_b + \Delta p$, where the pressure drop across the catheter of pipe friction coefficient λ is given by the Darcy-Weisbach formula for pressure drop across circular pipes.

$$\Delta p = \lambda \times \frac{l}{D} \times \frac{\rho}{2} \times \dot{x}_2^2, \tag{2}$$

The resulting dynamical equations for the micropump takes the form of a nonlinear lumped model approximate ODE:

$$m\ddot{x}_1 + kx_1 + (p_b + k_3 \dot{x}_1^2) A_1 = F. \tag{3}$$

Flow simulations for a micropump/check-valve/catheter system were carried out in *MATLAB*. Assuming a sinusoidal signal to the MEMS actuator with frequency $f = 50 \text{ Hz}$ (close to the thermal bandwidth of the MEMS actuator), and amplitude $F = 6 \text{ mN}$ we obtain the output flow rate of the pump.. Simulation results indicate that an average flow rate of $85 \text{ }\mu\text{l/min}$ can be achieved against a venous pressure of 8 mmHg . The previous fluid flow characterization was carried out on an unpackaged micropump. We are interested in knowing how the fluid flow is affected by the packaging the micropump. We make a simplifying assumption on scaling of the flow with respect to the pumping membrane force. Since the displacement-force relationship from equation (1) is quasi-

linear, if the pumping force F scales up by a factor of α , the pumping displacement, e.g. the flow rate will also scale up by the same factor. Therefore, a force reduction factor $\alpha=2.16$, will lead to a corresponding flow rate reduction of $\frac{85}{\alpha} = 39.33 \mu\text{L}/\text{min}$ for a packaged micropump.

E.5 Implantation model for the micropump

In this section, we use the macro-model to prepare an approximate implanted model of the micropump. The implant environment is assumed to possess similar thermophysical properties as water (the human body is 90% water). The steady state results for heat flux inputs equivalent to 8 and 10 V input power are presented in Figures 28 and 29 respectively. The outer layer of the body simulating the water volume is maintained at 36.8C. Figure 28(a) presents the result of steady state thermal analysis of approximate an implanted micropump model (complete package including the implant environment), while Figure 29(b) shows the temperature distribution for the implant environment alone. The input heat flux for the results presented in Figure 28 is equivalent to 8 V input voltage.

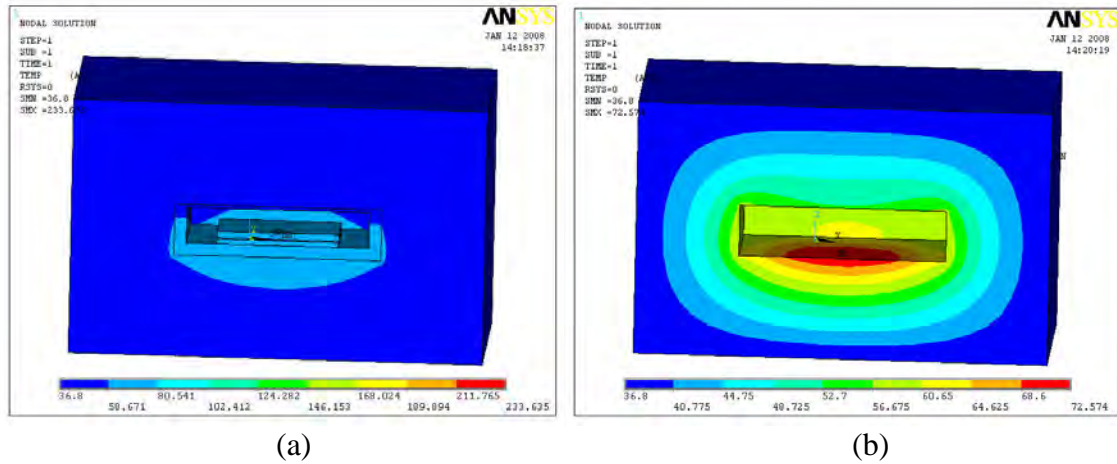


Figure 28: Steady state thermal analysis of approximate implanted micropump model (a) complete package and (b) the implant environment. Input heat flux is equivalent to 8 V input power.

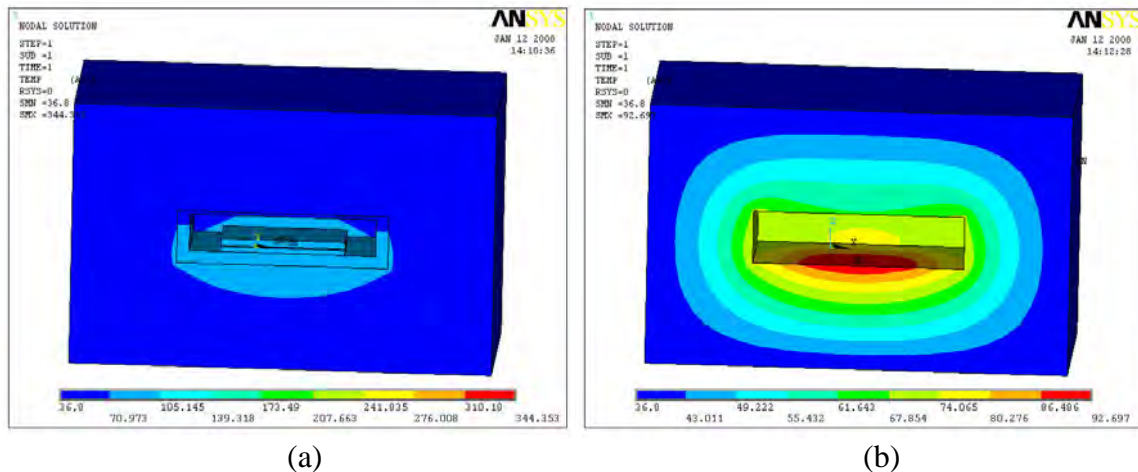


Figure 29: Steady state thermal analysis of approximate implanted micropump model (a) complete package and (b) the implant environment. Input heat flux is equivalent to 10 V input power.

Figure 29(a) presents the result of steady-state thermal analysis of an approximate implanted micropump model (complete package including the implant environment), while Figure 22(b) shows the temperature distribution for the implant environment alone. The input heat flux for the results presented in Figure 29 is equivalent to 10 V input voltage. From these results, we observe that the implant environment is exposed to high temperatures (72.6 and 92.7 C) respectively. These temperature values are in excess of the 40.8 C requirement for implantation inside the human body, hence we need to redesign the package.

E.6 Micropump Package Redesign

The initial micropump package was implemented using a Kovar carrier in order to reduce the thermal mismatch between the micropump's SOI die and the carrier. This package was found to be inadequate in the previous section since the steady-state temperature distribution on the outside of the carrier exceeds 106 °C as shown in Figure 30. In order to meet the outside temperature requirement, modification to the package design is necessary. We propose a package modification consisting of polybutylene terephthalate (PBT) outer package with locating pins that constricts the movement of the inner Kovar carrier as shown in Figure 31. With this modification, we simulated a maximum outer temperature of about 40 °C on the micropump's outer surface. While the new design may not be optimal, it indicates that a parametric design for the package is possible using the lumped model.

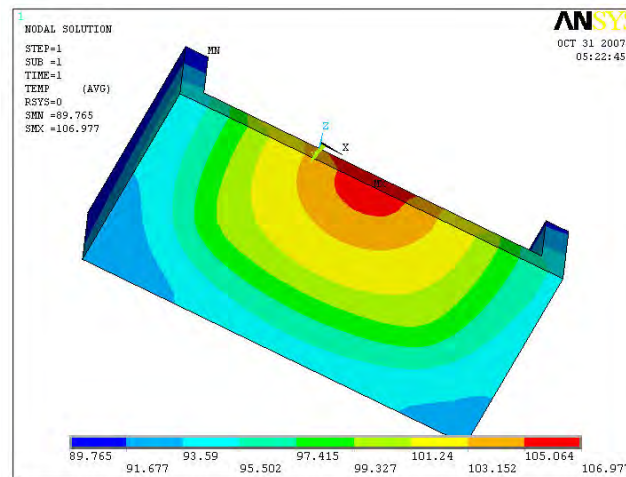


Figure 30: Temperature distributions on the original Kovar carrier.

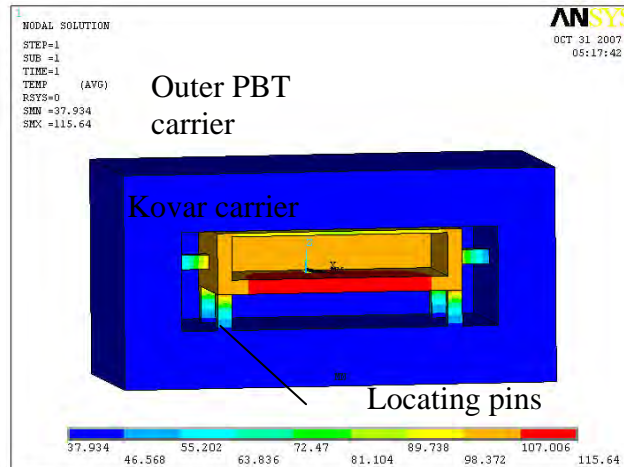


Figure 31: Temperature distributions on the modified micropump package.

Micropumps are classic examples of MEMS packaging challenges. In this report we discussed packaging aspects related to a novel Implantable Drug Delivery System (IDDS) that includes an electrothermal microactuator. In addition, the IDDS requires multiple interconnection types (fluidic and electrical). It has to be bio-compatible with the host environment (human body) and should not dissipate too much heat to the surrounding environment. In particular, the requirements of this device for implantation include a temperature increase outside the package by only 4°C. The device should dispense precise amount of medication at expected times and there must be no leakages. Hence the need for hermetic sealing of the package. The packaged device must be small and not cause much discomfort to the user.

We presented simulation of the packaged and unpackaged micropumps based on reduced-order lumped model approximations. The most error obtained is less than 10% (for the electrothermal analysis of the packaged micropump) with computational time reduction from about 8 hours (using ANSYS® solid98 coupled field elements to a few minutes (using solid87 thermal elements). Based on the results from the thermal analysis, package modification was deemed necessary in order to maintain package outside temperature no more than 40.6°C. Our approach is shown to be accurate and efficient and can be used for the analysis of packaged electrothermal MEMS actuators in general. In the future, additional optimization based on parametric studies will be carried out using the macro and micro-models.

Although more work needs to be completed in implementing a packaged implantable micropump for use in cancer treatment, the analysis and experiments presented in this report clearly show that such a micropump is technically feasible.

F. Micropump package for cancer delivery studies

In order to test the effectiveness of the micropump with cancer drugs and construct appropriate animal models we combined driving circuitry, power and a pump into a table-top hand held unit prototype that is shown in Figure 32. Even though this prototype is not

yet fully miniaturized and not ready for implantation, it can be used can deliver a controlled flow rate of 7-140 $\mu\text{l}/\text{min}$ to a cancerous tumor intravenously and will enable us to achieve Aim 4 of this project.



Figure 32: External pump module with control unit that will be used in future testing

The pump is set for maximum flow 140 $\mu\text{l}/\text{min}$ for a delivery tube diameter of 0.02". The flow rate can be altered by changing the potentiometer in the circuit (arrangements can be made to make this easily accessible). Another method to alter the flow rate is to change the interconnect tube dimensions, and the pump needs to be primed before operation. That is, there should be some fluid injected in the tubing before the pump operation is started. Once the flow has been established this need not be repeated unless the fluid in the reservoir is depleted. The reservoir may be open or closed type. There are toggle switches with LED indicators for ON (RED) and OFF indication.

Results of research towards Aim4 from co-PI Liu and PI Popa

Objective: To study the relationship between drug release rate, tumor oxygen levels and therapeutic outcome. We study the effects of using different drug delivery rates with a micropump to the effectiveness of the treatment.

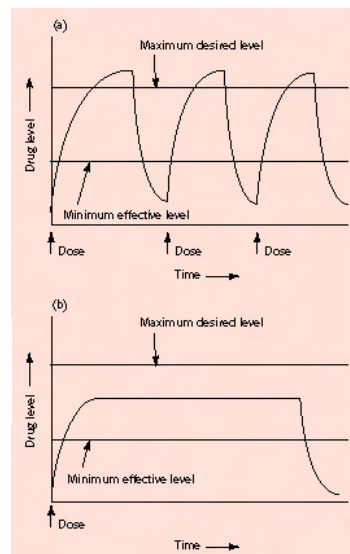
A. Introduction

Drugs administered via conventional techniques target not only the diseased cells but also the healthy cells. Oral medications, injections and capsules are the most frequently used techniques. These techniques rely on blood flow to carry the drug to the targeted organ or cells. To ensure complete cure, the dosages required are higher and stronger and can have severe side effects. Methods to deliver a drug locally in order to make it more potent have been extensively studied and documented in the past. Gelatin coated pills, compressed pills minimized the side effect of drugs; however they still rely on the uptake of the drug into the circulatory system through the stomach and intestinal lining. Targeted or localized drug delivery using polymer stents, drugs coated with polymer that are biodegradable or water soluble have been proposed and have been approved for use in various treatments. The need to appropriate modulation of the delivery rate is required to maximize the therapeutic effects with low toxicity.

Drug delivery rates for drugs to be effective must maintain a specific level between the minimum required and maximum level below toxicity at all times during the course of administration. There are several factors that determine the rates at different stages of the disease. The drug dosage administration is as depicted in Fig. 1. The key parameters that should be optimized for drug delivery are a) selectivity of drug action b) interval between administrations drug dose and c) probability that the next dose is administered at the appropriate time.

Chemical stability, reaction with drugs, body fluids and temperature effects are studied to determine the best suited materials. There exist standards for determining biocompatibility of polymers. For example, the biocompatibility tests for Polyethylene are given by the ASTM standards F981, F639, F755.

**Figure 1: Drug levels in the blood with
(a) traditional drug dosing and (b)
controlled-delivery dose.**



B. CCD Measurements of Tumor Oxygenation

To accomplish Aim 4, we started our animal measurements using the CCD camera. Figure 2(a) shows the setup of the CCD camera, and the relative position between the

camera and rat tumor. Figure 2(b) shows a close look of the rat prostate tumor and four fiber bundle tips that were used to deliver light. The prostate tumor line was R3327 AT3.1, and it generally took 7-10 days to have the tumor appear on the animal foreback.



Figure 2(a) Experimental setup for animal study.

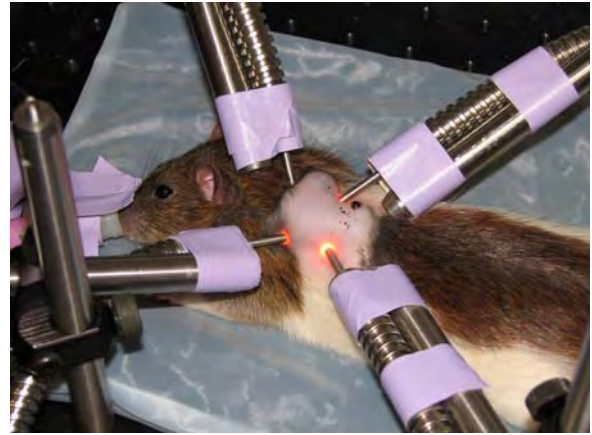


Figure 2(b) A Copenhagen rat with a prostate tumor grown on the foreback. Four light-delivery fiber bundles are in good contact with the tumor for the NIR measurement. The four probes were held through the metal optical posts, as shown.

A dosage of 200 mg of Cyclophosphamide (Sigma-Aldrich, Inc) per kilogram of rat body weight was initially used to investigate the primary effects of the drug. The drug was injected through ip when the tumors appeared to be 1.5 cm in diameter. Continuous recordings on the animals' tumor size and body weight were done daily after the drug injection. Figures 3 (a) and (b) show the corresponding changes in tumor volume and percentage decrease in rat body weight, for two control rats and two treated rats. It appears that the treated rats have a slower rate in tumor grow and in body weight lose in comparison to the control rats. It also suggests that the dosage of drug seems to be a little low, and it is reasonable to expect that a higher dosage of drug could stop the tumor grow. However, whether or not a higher dosage would lead to a toxic effect on the animal remains to be investigated through the rest of the funding period. We are currently carrying out the continuous study with more animals and more detailed measurements.

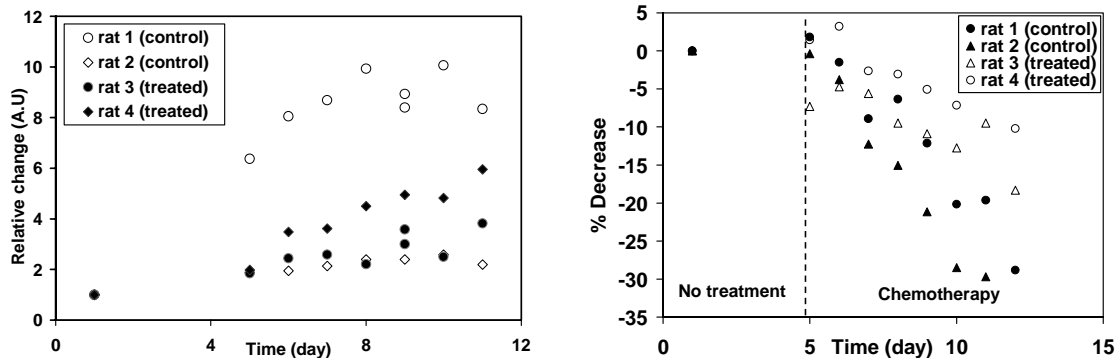


Figure 3. Changes in tumor volume with time (a) and changes in rat body wt. with time (b)

Furthermore, we employed the CCD camera, as shown in Figures 3(a) and 3(b), to detect and quantify the hemodynamic changes of the prostate tumors under oxygen intervention. The protocol for oxygen intervention is given as follows: 10 minutes for baseline recording while the rat breathed air, followed by 10 minutes of oxygen breathing for the rat, and then switched back to air for another 10 minutes. We expect to see different dynamic responses to oxygen intervention between control and treated rat tumors, and such dynamic responses can provide us with information on therapeutic effects and efficacy of the drug. Figure 4 shows an example of such a hemodynamic response of a prostate tumor to oxygen, and this figure is obtained by averaging the tumor region.

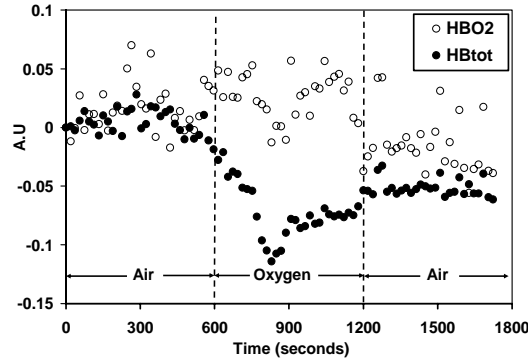


Figure 4. Hemodynamic changes in the tumor region during gas intervention

Furthermore, Figures 5(a) and 5(b) illustrate topographic maps of oxygenated hemoglobin concentration of the tumor during the periods of baseline and oxygen intervention, respectively. Figure 5(b) basically shows that some regions of the tumor have a large increase in oxygenated hemoglobin (HbO), represented by red color, and some regions do not show (or have small) changes in HbO. The color scale given on the right hand side of Figure 5(b) gives the quantitative representation of the HbO values, while the values of the color scale are in arbitrary unit for a relative comparison. In short, both. Figures 5 demonstrates that we have established an effective imaging tool to be used in studying tumor heterogeneity in response to chemotherapy and the relationship among the drug dosage, tumor oxygenation and therapeutic outcome.

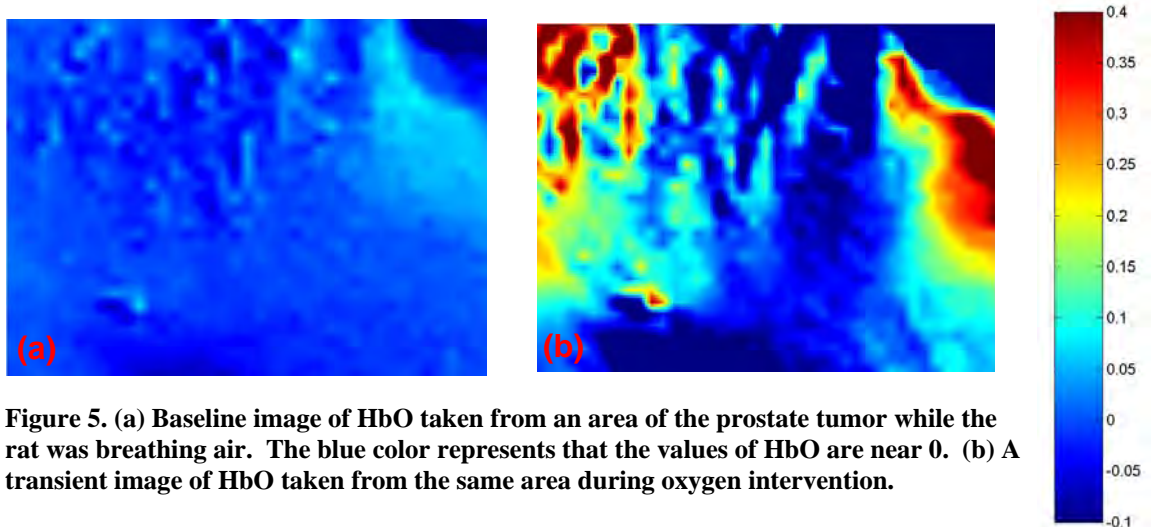


Figure 5. (a) Baseline image of HbO taken from an area of the prostate tumor while the rat was breathing air. The blue color represents that the values of HbO are near 0. (b) A transient image of HbO taken from the same area during oxygen intervention.

C. In-vivo Evaluation of Drug Delivery using a Micropump

Cancer research is a multifaceted area of study which is in no way limited to investigations designed to assess the carcinogenic or, indeed, anti-carcinogenic potential of chemical compounds. Despite the range of studies involved, one common factor necessary for the success of these investigations is the ability of the researcher to control the delivery of the agents under study, in a precise and dependable manner. Infusion and injection are a few of the many existing means of delivering these drug agents as seen in the Figure 6.

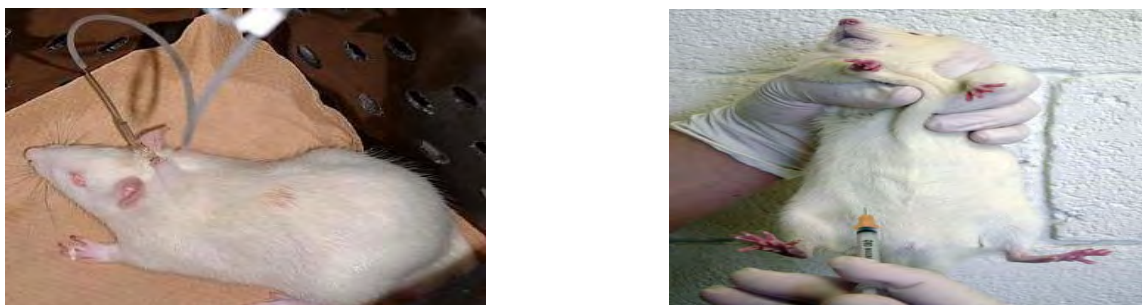


Figure 6. Different means of drug delivery (pump-left) and (injection-right)

During this research, it was not be possible to implant our prototypes into Copenhagen rats for testing, due to their large sizes. Instead, we connected the prototype through intravenous ports or directly to the tumor tissue, and control the drug delivery rate. But delivering drugs at a constant rate is the key to reduce side effects and increase efficacy. To demonstrate a drug's efficacy, it must reach the target tissue (cancerous region) at a concentration sufficient to elicit a therapeutic effect.

Infusion pumps are well-known, implantable devices used for infusing fluids i.e. the drug into the circulatory system. For the comparative study of drug delivery at a constant rate, two types of pumps were used in in-vivo studies with rate. One of them was an external IDDS micropump, and the other being the internally implanted osmotic pump as seen in Figure 7. The internally implanted pump was purchased from Alzet Osmotic pumps. Whereas, the external micropump was from the Original Equipment Manufacturers (OEM's) Instech Laboratories Inc. Both of them deliver drugs to the targeted area at a predefined flow rate.



Figure 7. Osmotic Pump

The osmotic pump operates due to the osmotic pressure difference between a compartment within the pump, called the salt sleeve, and the tissue environment in which the pump is implanted. As the water enters the salt sleeve, it compresses the flexible reservoir, displacing the test solution from the pump at a controlled, predetermined rate.

C1. Description of Experimental Method

Experimental Set 1:

A total of eight Copenhagen rats weighing between 200-300 gms were grouped in four different groups as follows:

- Group 1- Control rats (Injected with tumor and no treatment) (2)
- Group 2- Injection treated rats: (2)
- Group 3- Rats treated using the osmotic pump (2)
- Group 4- Rats treated with IDDS MicroPump (2)

Once the rats were injected with cancer cells, the weight of the rats; size and the spectroscopic reflectance using a spectrometer, of the tumor were measured. NIR (Near infrared Spectroscopy) has been investigated as a possible technique to differentiate between normal tissues and tumors. Measurements of reflectance using an optical probe gives an effective attenuation, which is the product of the optical properties obtained from the slope of the reflectance. A combination of spectral features and slope features obtained could provide vital information, to localize target tissues. After a week's watch of the growing tumor, the different treatment of the six rats was started. The drug used for treatment was cyclophosphamide, with the concentration of 1.68 mg/ml. Cyclophosphamide is a "prodrug" used to treat various types of tumors. The second groups of rats were injected with the above concentration of the drug. In the third group of rats, the osmotic pump was infused surgically into the subcutaneous layer of the skin and was connected to the tumor area through a catheter. Lastly, the fourth group rats were injected with the drug through the external micro-pump, whose flow rate was predetermined. The drug flow time for the pump was roughly two hours.

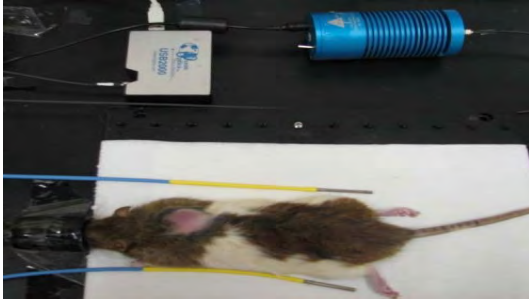


Figure 8. Experimental Set-up

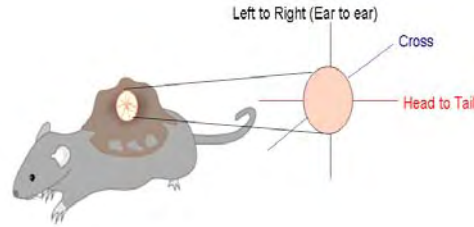


Figure 9. Measurement of tumor size



Figure 10. External IDDS Pump treatment



Figure 11. Internal pump treatment

Figures 8-11 depict the experimental measurements of tumor size, oxygenation, and the infusion of drugs using the two pumps.

Experimental Set: 2

To derive improved and conclusive results, this study was replicated by providing treatment to the rats using the external pump after tumor injection as early as the third day of tumor injection. The rats were grouped as follows:

- Group 1: Control rats (1)
- Group 2: Injection treatment (2)
- Group 3: Early Pump treatment (2)
- Group 4: Late treatment using the micropump (1)
 - : Late treatment using the jacket for drug delivery (1)

The early pump treatments were started on the day when the tumor size approximately reached 1.5 cm. The late and early treatments, using the micropump were categorized in order to see the effect that, the starting of the pump treatment showed any significant difference. The early pump treatment was started 4 days prior to the late pump treatment. The drug concentration was kept the same as in the earlier trial, but was divided over 4 days for daily treatment in both the early and late pump treatment, which was not in the case of previous set. The run time for the pump on each of the days was approximately 30 minutes. The spectroscopic set-up was also kept the same, and three measurements on the tumor were made as shown in the figure. The source detector separation was kept constant at 1cm at an integration time of 300ms in the OOIBase software used for spectroscopic measurements (Figure 12).

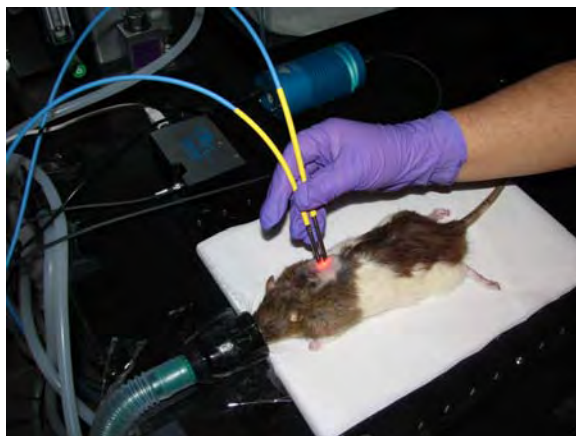


Figure 12. Spectroscopy measurement.

For the late treatment of the pump an infusion harness kit (Figures 13, 14) was used in order to keep the rat in a conscious state during drug delivery. The infusion harness jacket kit for rats was purchased from SAI infusion. The set-up for the treatment is shown in the figures below. The kit was coupled to the micropump through an adjustable catheter, which permitted the free movements of the rats inside the cage. The body weight and the tumor size measurements were monitored constantly

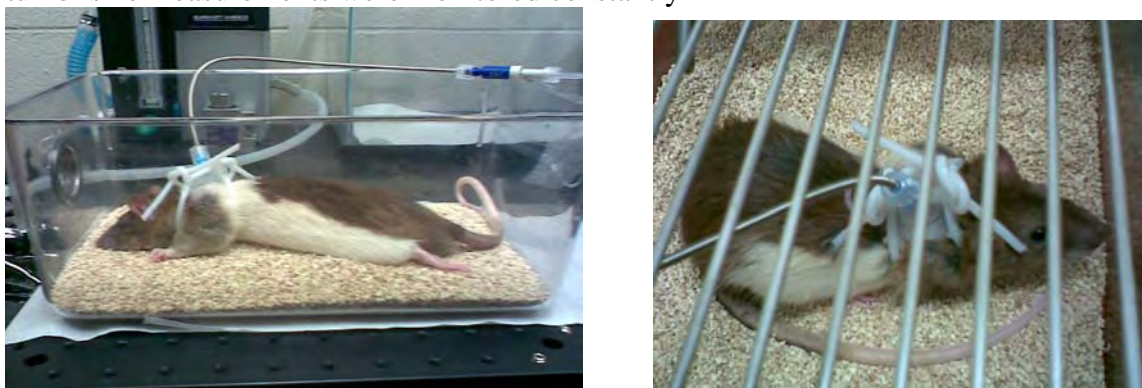


Figure 13. The use of infusion harness kit for treatment

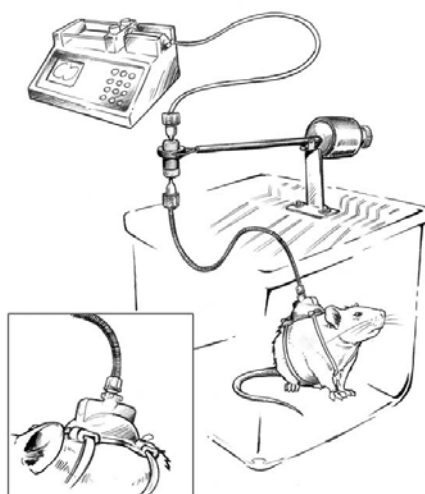


Figure 14. Depiction of the infusion harness kit

C2. Experimental Results

Results for Set :1

The graphs in Figure 15 depict the body weights and the tumor size of the rats before and after the treatment.

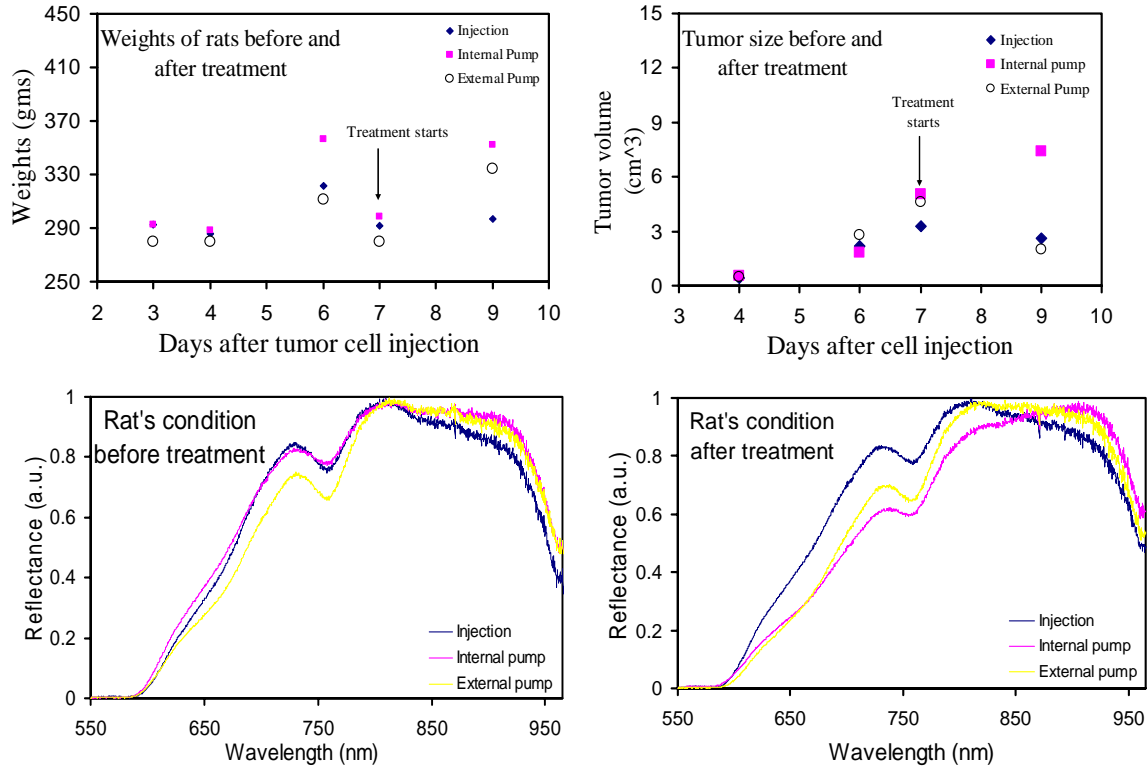


Figure 15. Measurement of body weight and tumor size along with the comparative spectroscopic measurements of before and after treatment.

The reflectance measurements from the rats undergoing various forms of treatment were also analysed as shown in Figure 16, depicting the reflectance spectrum of the rat tumor tissue before and after treatment with the two micropumps.

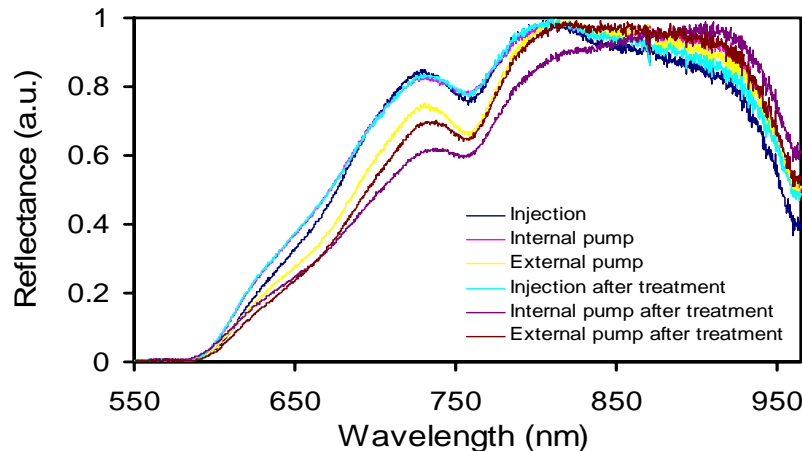


Figure 16. Spectroscopic measurements for all the different treatments.

For the first trial, the comparative study indicates that the use of the external pump (the IDDS) indeed shows significant changes in terms of the tumor volume and the body weights of the rats. From the experimental results, it is seen that the body weight increases after treatment or infusion of the cyclophosphamide. Also, the tumor volume decreases significantly after the conventional injection treatment. This effect is largely seen in the external pump, which is one of the proposed effective means of drug infusion. Since, this is the first study, the results presented here should be considered preliminary. The impact of a conclusive comparative study would need a bigger data set.

Results for Set: 2

The graphs in Figures 17 and 18 depict the body weight and the tumor size of the rats for the second set of experiments. Also, the ratio of the deoxygenated to the oxygenated hemoglobin are shown, i.e the ratio of the peaks in each of the spectrum. In the body weight graphs the first day indicates the day of tumor injection. Whereas, in the case of tumor size, the size was measureable only after the third day of tumor injection.

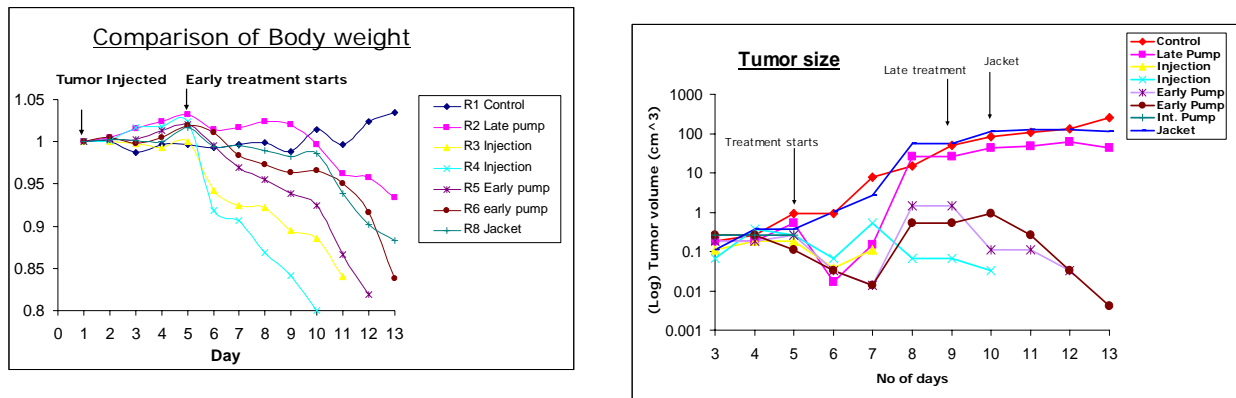


Figure 17. Graph of body weights and tumor size over days

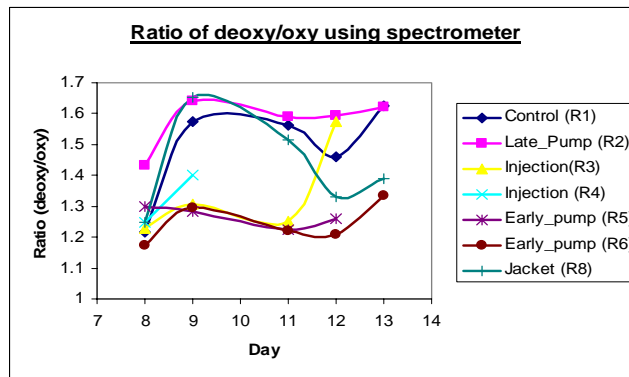


Figure 18. Graph of the ratio of deoxygenated to the oxygenated hemoglobin

The tumor size measured over days follows a logarithmic scale. The spectrometric measurements were taken over the 8th day after the tumor injection.

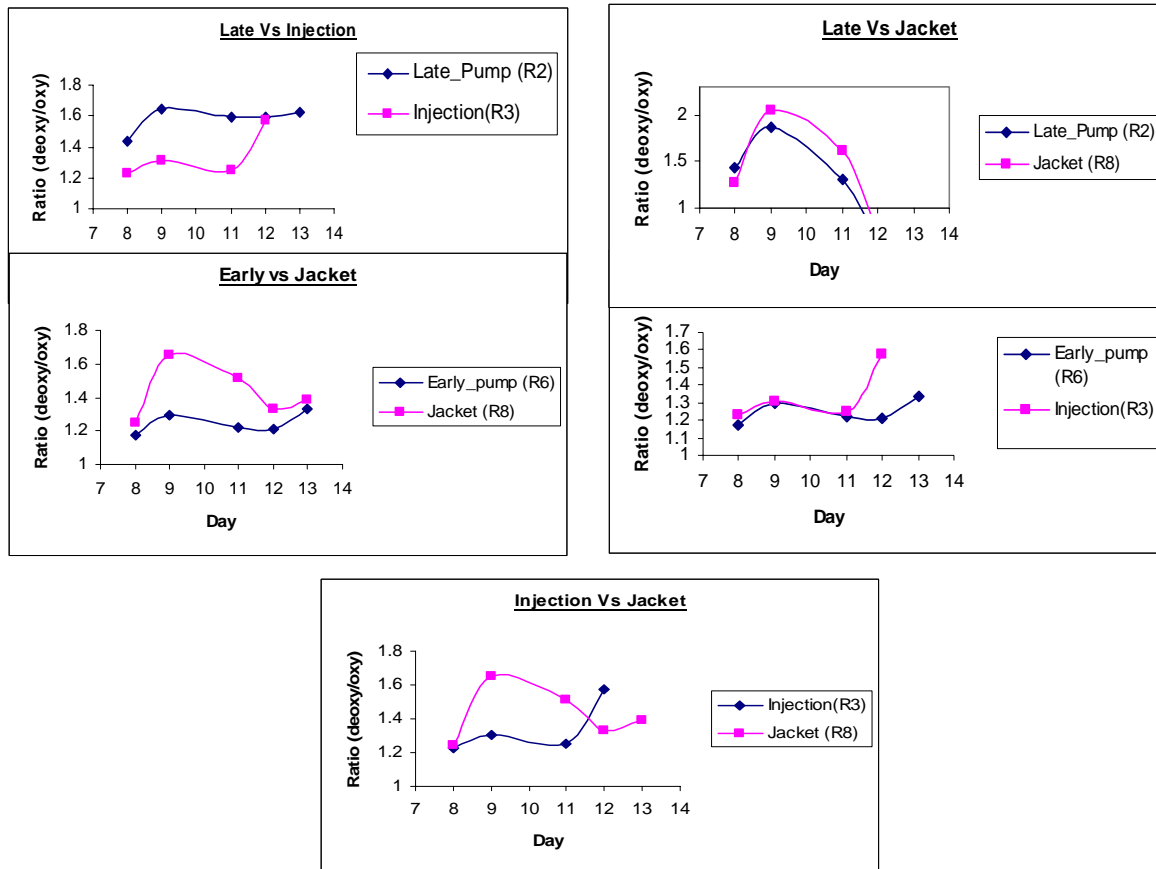


Figure 19. Comparative spectroscopic measurements of different groups of treatments.

In Figure 19, comparative spectroscopic graphs of the ratios were also plotted to indicate the difference between the different group of treatments.

For the second experimental trial, the set was replicated with an earlier treatment using the external pump as compared to the first trial. In case of the tumor volume, the size shrinks after the onset of the treatment for injection and the external pump treatment. As seen in Figure 19, for tumor size, the late treatment using the pump and jacket were started when the tumor size was of an appreciable size of 1.5-1.7 cm³ and hence the treatment did not show much efficacy. But in the case of early treatment of the external pump and injection, the treatment was started on the third day after the tumor injection and the efficacy of the treatment is indicated by the shrinking of the tumor size. **We can conclude that the early treatment with the external IDDS micropump proves to be more effective than late treatment.**

D. Protocol for Animal Testing

During this grant we developed a new animal protocol for experiments conducted on Copenhagen rats. The protocol describes: tumor growth, anesthesia, surgery for micropump/catheter implantation, blood oxygenation measurements, and drug infusion. In this section, we list excerpts from the protocol submitted and approved by UTA's Live Sciences Lab.

Protocol Narrative:

State: (i) sources consulted, e.g., Biological Abstracts, Index medicus, Medline, the Current Research Information Service (CRIS), Animal Welfare Information Center (AWIC); (ii) the date of the search; (iii) years covered by search and (iv) the key words and/or search strategy used.

Medline search from year 1966 through 2006 was performed on 10/26/2006 using the following key words: Prostate tumor, local chemotherapy, animal models, light reflectance, fluorescence, CCD camera, prostate tumor + local chemotherapy, prostate tumor +local chemotherapy + animal models, prostate tumor +local chemotherapy +light reflectance, prostate tumor + local chemotherapy +CCD camera, prostate tumor + local chemotherapy +fluorescence. The outcome of search revealed that the proposed work does not unnecessarily duplicate previous research.

Alternatives to any procedure that may cause pain or discomfort have been considered and searched on 10/26/2006 via the Animal Welfare Information Center and Medline. The key words used were chemotherapy, prostate tumor, animal models, safety.

Species: Rat

Strain/Stock: Copenhagen rats

Source: Harlan

USDA Vendor:

Yes

No

Duration of project (years): 2 Years

☒☐

Maximum # of animals to be housed at one time: 20

Estimated number per year: 30

Total through course of project: 35

Procedures performed on animals: In the space provided, give a brief layperson's description of the procedures performed on animals in this project. Provide page # of continuation if needed.

Tumor growth:

Prostate tumor cells will be injected into the subcutaneous tissue in the thigh or on the fore back of male rats under gas anesthesia. The tumors will be grown under the investigators' monitoring, and the tumor diameters will be measured every other day to determine the volume. As soon as the tumor appears visually, the tumor will be ready for the pre-treatment measurements by the optical methods.

Optical methods to be used in the study:

There are four optical methods to be used in this study to measure prostate tumors in vivo before, during, and after the drug treatment:

- 1) light scattering reflectance using a small source-detector separation probe;
- 2) diffuse light reflectance using a large source-detector separation probe;
- 3) auto-fluorescence spectra using a small source-detector probe;
- 4) CCD-camera-based, light reflectance measurements.

Optical measurements by the optical methods prior to and after drug treatment:

There are two steps for the optical measurements:

- 1) Completely non-invasive measurements using the 4 methods mentioned above.

The rats with an appeared tumor will be anesthetized with pentobarbital (50 mg/Kg) and maintained under general gaseous anesthesia with 1.3% isoflurane in air (1 dm³/min). Tumors will be shaved to improve the optical contact for the near infrared measurement. A pulse

oximeter will be placed on the hind foot to monitor arterial oxygenation. The rat will be placed on a temperature-controlled, warm blanket to keep the animal's body temperature. The optical probes for light delivery and detection will be held to have a good contact with the tumor surface. Inhaled gases may be alternated in the sequence of air-oxygen-air. The reason to use oxygen as intervention is to study the effects of interventions on prostate tumor oxygenation, so as to study the effect of tumor oxygenation on therapeutic outcome.

Bifurcated fiber-optic probes with a diameter of 1.2-1.5 mm can be placed on the surface of tumor or other parts of the animal body non-invasively to record light scattering reflectance or auto-fluorescence. A larger fiber-optic probe with a diameter of 2.5 cm can be used in the similar fashion to read diffuse light reflectance from the tumor or normal control tissues from the experimental animal. The same experiments can be taken using a CCD camera. Both light scattering reflectance and auto-fluorescence provide us with distinct signatures between control and cancer tissues, and the differences between treated and untreated tumors. The diffuse reflectance and CCD camera readings will permit *in vivo* calculations for tumor vascular oxygenation and total hemoglobin concentrations. The heterogeneity of tumor vascular dynamics will be compared with that in drug-treated tumors. The tumor size and life span of each rat will be recorded as statistical data for final analysis.

2) Invasive measurements of the prostate tumors in vivo before sacrificing the animals.

To understand the effects of rat skin on the measured optical signals, we will take only light reflectance and auto-fluorescence (no CCD-camera readings) from the exposed prostate tumors *in vivo* after opening the skin on top of the tumor. This step will take place only at the last stage of the living animal. The rat will be under general gaseous anesthesia with 1.3% isoflurane in air (1 dm³/min), and the skin on top of the tumor will be cut and separated from the tumor so that the surface of tumor will be exposed for measurements. The bifurcated probes will be placed on the exposed tumor surface, and the reflectance and auto-fluorescence signals will be recorded at multiple locations. In this case, no gas intervention will be given. After the optical readings are complete, the tumor will be excised for further measurements, and the rat will be sacrificed using CO₂ chamber.

The above measurement procedures will be used for both the control group and the drug-treated group. Both treated and untreated rats will be observed on a daily basis and will be sacrificed if the tumors are growing too big (larger than 3 cm in diameter) or bleeding greatly. The removed rat tumors will be put in either formalin or PBS for pathological analysis. If any of the following signs occurs in the animals, i.e, stop eating, stop grooming, decrease in body weight by 20%, distress or pain, the animals will be immediately euthanized.

Histological analysis of the treated animals

Once the rat prostate tumor is removed from the animal's body, it will be placed in formalin or PBS solution in preparation for histological assessment or other ex vivo optical measurements. The histological analysis will be performed in Co-PI Tang's laboratory, and the ex vivo optical measurements will take place in both co-PI Liu's laboratory and at the University of North Texas Health Science Center at Fort Worth for time-resolved, auto-fluorescence measurements.

Setup and Measurements of the NIR Hemodynamic Imaging of the Rat Prostate Tumor

CCD Camera: To have a better spatial and temporal resolution, we have implemented a multi-wavelength, CCD camera for the study. A CCD Camera with a 12 bit CCD array focuses on the animal's tumor. There is a mechanical wheel positioned in front of the CCD camera to hold 6 filters at the NIR wavelengths between 650 nm and 850 nm for multi-spectral measurements. The

illumination light (including the NIR region) will be delivered through a broadband light source from the sides of the tumor. A pair of linear light polarizers may be added in front of the light source and the CCD camera to improve the light penetration depth into the tumor tissue. The collected CCD signals will be converted to the electrical signal, then passed on to the computer to be processed and displayed. LabVIEW™ programming software will be used as the interface software between the camera and computer to display the scattering index information.

Probe-based reflectance and auto-fluorescence measurements: The probe is bifurcated and has an outer diameter of 1.3 mm. The two bifurcated branches are connected to a light source and a CCD-array spectrometer. During the experiment, the probe will be placed gently on the skin of the tumor for data collection. The measurement will be repeated at multiple sites on the tumor and a chosen area of muscle for comparison. Such measurements will be continued for a few days, followed by open-skin measurements before sacrificing the animal. For good statistics, we plan to use 12 rats for a high dose treatment, 12 for a low dose treatment, and 6 for the control group.

USDA Classification of animal use (see INSTRUCTIONS attached)

1.1.1 Project Period		Number of Animals by Category:			
From (mo/yr)	To (mo/yr)	1	2	3	4
October 2006	Sept 2007			25	
Sept 2007	Feb 2008			10	

Special requirements for maintaining Animals:

Yes
☐

No
☒

If yes, indicate the requirements below, such as caging, bedding, type of water and dietary requirements. If no, animals are to be maintained according to the standard operating procedure of the animal facility.

Other special instructions for animal care staff:

Instructions for treatment and disposition of animals:

Illness		Death		Pest Control	
Call Investigator	<input checked="" type="checkbox"/>	Call Investigator	<input checked="" type="checkbox"/>	None	<input type="checkbox"/>
Treat	<input checked="" type="checkbox"/>	Necropsy	<input type="checkbox"/>	Veterinarian's Option	<input checked="" type="checkbox"/>
Terminate	<input type="checkbox"/>	Bag for Disposal or	<input checked="" type="checkbox"/>	Pyrethrin	<input type="checkbox"/>
Wild or exotic species	Yes <input type="checkbox"/> No <input checked="" type="checkbox"/>	Permits?	Yes <input type="checkbox"/> No <input checked="" type="checkbox"/>		

Invasive procedures (other than blood collection, catheterization, intubation, etc.)?.....Yes ☒ No ☐

a. If yes, will the procedure be done under anesthesia? Yes No ☒ ☐

- b. If yes, describe the anesthesia to be used including dose and route of administration.

The rat will be under general gaseous anesthesia with 1.3% isoflurane in air (1 dm³/min).

If no, explain in detail why anesthesia is not used:

- c. Person(s) responsible for post-anesthesia recovery?

The animal will be sacrificed after the invasive procedures. There is no need for post-anesthesia recovery.

Restraint (Chairs, slings, tethers, stanchions, metabolism cages or other devices).

Yes No ☐ ☒

Surgery:.....Survival ☐ Multiple ☐ Terminal ☒ None ☐

- a. Location (building/room) of surgical suite: UTA Animal Facility

- b. Surgical procedure(s):

The rat will be under general gaseous anesthesia with 1.3% isoflurane in air (1 dm³/min), and the skin on top of the tumor will be cut and separated from the tumor so that the surface of tumor will be exposed for measurements. The bifurcated probes will be placed on the exposed tumor surface, and the reflectance and auto-fluorescence signals will be recorded at multiple locations. In this case, no gas intervention will be given. After the optical readings are complete, the tumor will be excised for further measurements, and the rat will be sacrificed using CO₂ chamber.

- b. Anesthetics, analgesics, or tranquilizers used.....

Yes No ☒ ☐

The rat will be under general gaseous anesthesia with 1.3% isoflurane in air (1 dm³/min).

- c. Describe the post-operative care (survival procedures only):

The animal will be sacrificed after the surgery.

- d. Under what circumstances will incremental doses of anesthetics-analgesics be administered?

Animals will be under constant monitoring during the experiments; they will be checked regularly of the blinking reflex and the pupil reflex. If any sign of movement during experiment appears, the animal will be given an increased anesthetics.

- e. If neuromuscular blocking agents are being used without general anesthesia, provide justification:

Intervention for pain or distress...☒ analgesia ☒ euthanasia ☐ other

Hazards to personnel (if applicable):

☐ Radioisotope: None

☒ Carcinogen: Always wear gloves and lab coats when dealing with the animals.

☐ Biohazard

☒ Other Animal Bites, Animal Allergens, and sharps.

Body fluids or tissue from these animals may be utilized by other investigators.....

Yes No ☒ ☐

Describe: The excised rat prostate tumors may be taken to the fluorescence laboratory at the University of North Texas Health Science Center at Fort Worth for auto-fluorescence lifetime measurements. Such a measurement may help us with the new development on intraoperative optical methods to demarcate human cancers during laparoscopic surgery.

Detailed description of the procedures to which the animals will be subjected

Tumor growth:

Prostate tumor cells will be injected into the subcutaneous tissue in the thigh or on the fore back of male rats under gas anesthesia. The tumors will be grown under the investigators' monitoring, and the tumor diameters will be measured every other day to determine the volume. As soon as the tumor appears visually, the tumor will be ready for the pre-treatment measurements by the optical methods.

Optical methods to be used in the study:

There are four optical methods to be used in this study to measure prostate tumors in vivo before, during, and after the drug treatment:

- 1) light scattering reflectance using a small source-detector separation probe;
- 2) diffuse light reflectance using a large source-detector separation probe;
- 3) auto-fluorescence spectra using a small source-detector probe;
- 4) CCD-camera-based, light reflectance measurements with four light source delivery.

Optical measurements by the optical methods prior to and after drug treatment:

There are two steps for the optical measurements:

(a) Completely non-invasive measurements using the 4 methods mentioned above.

The rats with an appeared tumor will be anesthetized with pentobarbital (50 mg/Kg) and maintained under general gaseous anesthesia with 1.3% isoflurane in air (1 dm³/min). Tumors will be shaved to improve the optical contact for the near infrared measurement. A pulse oximeter will be placed on the hind foot to monitor arterial oxygenation. The rat will be placed on a temperature-controlled, warm blanket to keep the animal's body temperature. The optical probes for light delivery and detection will be held to have a good contact with the tumor surface. Inhaled gases may be alternated in the sequence of air-oxygen-air. The reason to use oxygen as intervention is to study the effects of interventions on prostate tumor oxygenation, so as to study the effect of tumor oxygenation on therapeutic outcome.

Bifurcated fiber-optic probes with a diameter of 1.2-1.5 mm can be placed on the surface of tumor or other parts of the animal body non-invasively to record light scattering reflectance or auto-fluorescence. A larger fiber-optic probe with a diameter of 2.5 cm can be used in the similar fashion to read diffuse light reflectance from the tumor or normal control tissues from the experimental animal. The same experiments can be taken using a CCD camera. Both light scattering reflectance and auto-fluorescence provide us with distinct signatures between control

and cancer tissues, and the differences between treated and untreated tumors. The diffuse reflectance and CCD camera readings will permit *in vivo* calculations for tumor vascular oxygenation and total hemoglobin concentrations. The heterogeneity of tumor vascular dynamics will be compared with that in drug-treated tumors. The tumor size and life span of each rat will be recorded as statistical data for final analysis.

(b) Invasive measurements of the prostate tumors in vivo before sacrificing the animals.

To understand the effects of rat skin on the measured optical signals, we will take only light reflectance and auto-fluorescence (no CCD-camera readings) from the exposed prostate tumors *in vivo* after opening the skin on top of the tumor. This step will take place only at the last stage of the living animal. The rat will be under general gaseous anesthesia with 1.3% isoflurane in air (1 dm³/min), and the skin on top of the tumor will be cut and separated from the tumor so that the surface of tumor will be exposed for measurements. The bifurcated probes will be placed on the exposed tumor surface, and the reflectance and auto-fluorescence signals will be recorded at multiple locations. In this case, no gas intervention will be given. After the optical readings are complete, the tumor will be excised for further measurements, and the rat will be sacrificed using CO₂ chamber.

The above measurement procedures will be used for both the control group and the drug-treated group. Both treated and untreated rats will be observed on a daily basis and will be sacrificed if the tumors are growing too big (larger than 3 cm in diameter) or bleeding greatly. The removed rat tumors will be put in either formalin or PBS for pathological analysis. If any of the following signs occurs in the animals, i.e, stop eating, stop grooming, decrease in body weight by 20%, distress or pain, the animals will be immediately euthanized.

Reason for selecting the species and justification of number of animals used

To accomplish our goals, we will develop novel methodology and conduct preliminary experiments using a prostate tumor model in rat. It is crucial to use an animal model because tumors are not isolated organs, but rather respond to central stimuli such as blood pressure and hormones and inflammation. Tumor physiology involves a complex interaction of vascular components, e.g., pressure, blood oxygenation, and blood flow. This requires investigation of a 3-dimensional living tumor *in vivo*. Cell culture or computer simulation cannot provide a realistic model for the interplay of host and tumor. Rat has been widely used in the biomedical research field and in the prostate cancer investigations, and we prefer to use a rat model over mouse model since the rat physiology is far more stable under anesthetic conditions, and the rat tumors represent a smaller burden with respect to their body weight in comparison to mice. In short, we plan to use rats because of 1) their size, 2) availability, and 3) established prior reports.

Results of research towards Aim 5 from co-PI Tang

Objective: to create appropriate cancer tumor animal models, that will guide the growth of cancer tumor in Copenhagen rats. These rats are then used to support all the experimental work in the project.

During this project we have successfully established reproducible prostate cancer animal model using cancer cell lines. Many of these animals have been used in the study of the development of imaging modality. Specifically, rat prostate cancer cell line R-3327-AT-3.1 was obtained from the American Type Culture Collection (Rockville, MA, USA). Cells were cultured in Dulbecco's Modified Eagle Medium DMEM supplemented with 10% Fetal Bovine Serum (Invitrogen, CA, USA) at 37°C in a 100% humidified atmosphere containing 5% carbon dioxide. The subcultivation ratio is 1:20 and the medium was changed every other day to ensure the fast growth of the cells. The prostate cancer cells are adherent cells, have spindle-like shape and grow really fast (Figure 1). The cells were subcultured when they reach 80% confluence (~ once every 4 days). Some of the cells were cryo-preserved in liquid nitrogen.

To create prostate tumor in animals, we used male Copenhagen rats with 150 grams body weight. R-3327-AT-3.1 cells were recovered from culture flasks and then adjusted to 1×10^7 /ml in PBS. Prior to implantation, rats were anesthetized with the inhalation of 1-3% of isoflurane and then shaved to expose back foreside skin. Following sedation, 100µl of cell solution (equivalent to $\sim 1 \times 10^6$ R-3327-AT-3.1 cells) were injected subcutaneously under the foreside skin. In about 7 to 8 days, tumor tissues were growing to ~ 0.5 -1.0cm diameter which is the perfect size for our imaging study. If needed, tumor growth rate would be reduced by injecting lesser R-3327-AT-3.1 cells. Similar tumor can also be created by implantation prostate tumor tissue freshly isolated from other animals. Our results have shown that the implantation of tumor tissue has worse reproducibility than injection of cancer cells.

To ensure the quality of our cancer tissue, we often carried out H&E histological examination of the implanted prostate tumor tissue (Figure 2). Typically, prostate tumors possess the following characteristics: rapid cell growth, dense cell tissue, and good microvascular density. We believe that this animal model provides excellent in vivo system to study the imaging modality proposed in this project.

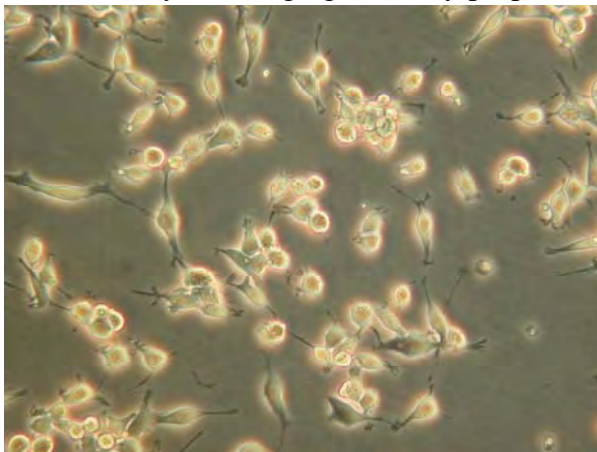


Figure 1. Morphology of R-3327-AT-3.1 (low density) under phase contrast microscope, 24 hours after being thawed from liquid nitrogen, 200X.

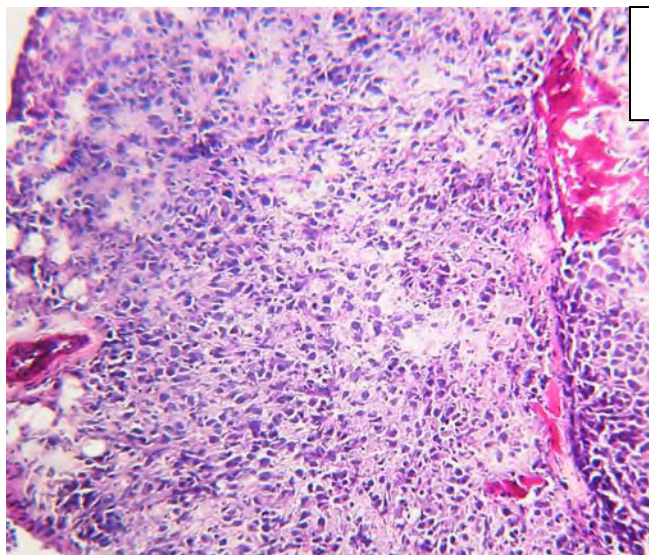


Figure 2. Histology of R-3327-AT-3.1 tumor tissue, H&E staining, 100X.

In this project, we wanted to create appropriate cancer tumor animal models, that will guide the growth of cancer tumor in Copenhagen rats. These rats are then used to support all the experimental work in the project. We have successfully established reproducible prostate cancer animal model using cancer cell lines. Many of these animals have been used in the study of the development of imaging modality.

In addition to this effort, co-PI Tang has been focusing on developing alternate chemotherapeutic treatments based on Quantum Dots (QDs). Due to their strong luminescence even under hypoxic conditions and photostability, QDs has drawn intensive research effort for their use as a cell label in medical imaging. To improve the cancer tissue specificity, QDs have been developed to target tumor by active or passive targeting mechanisms. One of the seminal studies on active targeting showed that QDs labeled with the protein transferrin underwent receptor-mediated endocytosis in cultured HeLa cells. These studies have shown that conjugating the quantum dots with a suitable receptor facilitates intracellular uptake by receptor mediated endocytosis. In addition, most of the tumor cells have no specific markers. Furthermore, there are no specific markers which could be used to target all or most tumor cells. Thus, more efforts should be expended in developing passive cancer targeting strategies. Our recent studies have found that maximal cellular uptake of nanoparticles occurs with nanoparticles measuring around 100 nm in size [71]. Based on these characteristics, our goal is to develop tumor targeting imaging probes by producing QDs embedded hydrogel particles (100 nm diameter).

Using a novel technology developed in our laboratory, we have been able to produce PNIPAM nanoparticles embedded with QDs and chemotherapeutic drugs. The functionality of these particles was then tested in vivo. Briefly, cancer cells ($1 \times 10^6/0.1$ ml/mouse) were implanted in Severe Combined ImmunoDeficient (SCID) mice. One week later, tumor tissues were observed on all the SCID mice back, with sizes of 0.5 to 1.0cm diameter. QDs (50ul) were injected into the tail vein of mice in one group while QD-NP with equivalent fluorescence intensity to QDs was injected in to the tail vein of mice belonging to the other group. Three hours following injection, the animals were

sacrificed and the tumor tissue was explanted and embedded in OCT (Optimum Cutting Temperature) for histological analyses.

The H&E staining images of the tumor sections show that there are no morphological differences among tumor tissue treated with either QDs alone (Figure 3A) or QDs embedded particles (Figure 3B). There were no sign of inflammatory responses or immune reactions. It suggests that both QDs particles and QD embedded particles are biocompatible. A closer look in to the tumor sections using a high magnification optical microscope showed a very scanty presence of luminescence in the case of QDs alone (Figure 3C) while a more intense luminescence was observed in the case of QDs embedded nanoparticles (Figure 3D). Since hydrogel nanoparticles can be incorporate with chemotherapy agents, we are in the processing of producing nanoparticles loaded with both QDs and chemotherapy drugs. It is our hope that in the future, this technology will simultaneously allow us to treat and to monitor tumor progression.

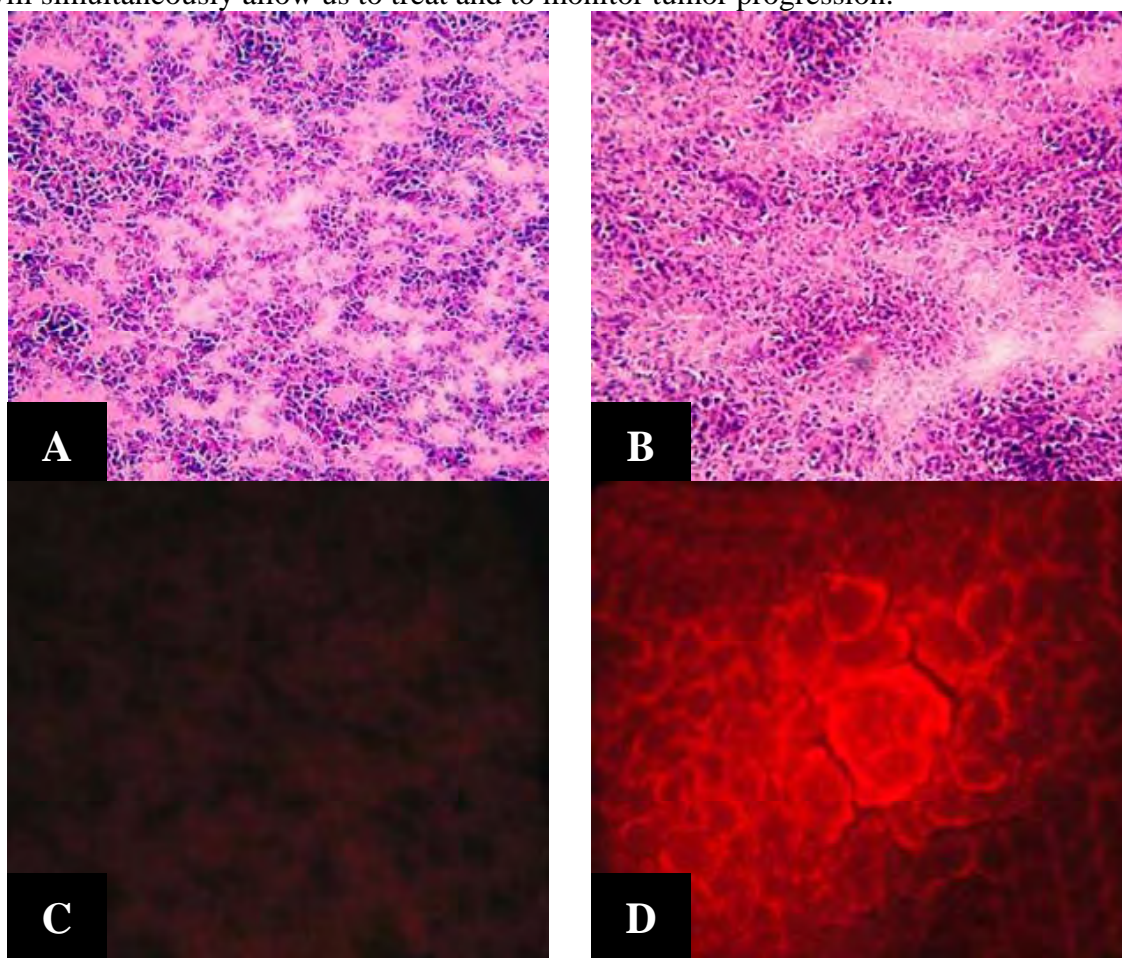


Figure 3 The H&E staining shows the similar morphology of tumor with quantum dots injected alone (A) and quantum dots embedded within nanoparticles (B) (Mag 20X). Quantum dots were observed under the fluorescence microscope; quantum dots injected alone in to the circulation are barely visible (C) while quantum dots embedded within nanoparticles are taken up in to the tumor and show up as bright red dots (D). (Mag 100X)

Key Research Accomplishments

- We have setup and calibrated a blood oxygenation measurement system using a high speed CCD camera to study the evolution of tumors.
- We have investigated the spectroscopic characteristics of
 - (a) light scattering,
 - (b) time-resolved auto-fluorescence,
 - (c) near infrared spectroscopy
 - (d) algorithm development to quantify hemodynamic parameters of animal prostate cancer tissue using respective spectroscopic systems.
- Using a novel technology developed in our laboratory, we have been able to produce nanoparticles embedded with Quantum Dots and chemotherapeutic drugs.
- We have designed and fabricated a novel IDDS micropump for controlled drug delivery of cancer drugs.
- We have studied the micropump flow rate and thermal dissipation through FEA and lumped parameter models for both the unpackaged and the packaged IDDS micropumps. Parts of the simulation model have been validated experimentally. The simulation models show drug delivery rates in the order of tens of milliliters per minute as required by cancer treatments with external pump units.
- We have refined fabrication and Level 0, 1, and 2 packaging processes for miniaturization of an implantable pump. A Level 2 prototype for drug delivery has been implemented. A complete finite-element analysis was performed in order to determine the impact of operating and design parameters like voltage, air gap thickness, substrate thickness, packaging and working fluid. All these parameters determine the maximum device temperature which in turn determines the maximum displacement and force of the diaphragm and the flow rate of the micropump.
- We have developed animal models for cancer tumor growth, and a new protocol for animal testing (tumor growth, micropump/catheter implantation, etc) at UTA's Live Sciences lab.
- We have conducted experiments studying the effects of drug delivery rate to the growth of tumors in Copenhagen rats. Preliminary results indicate that the treatment using larger drug flow rates (7-140 $\mu\text{l}/\text{min}$) lead to better tumor shrink rates, and fewer side effects than either injection or low-dosage treatments offered by implantable osmotic micropumps.

Reportable Outcomes

During the period 2005-2008, this grant supported several graduate students during their M.S. and Ph.D. studies. It supported the completion of a M.S. Thesis and a Ph.D. Thesis and the publication of several papers.

Journal Papers:

Nguyen KT, Shukla KP, Moctezuma M, Braden ARC, Zhou J, Hu Z, Tang L. In vitro studies of the cellular uptake of hydrogel nano- and micro- particles by phagocytes, vascular endothelial and smooth muscle cells. Journal of Biomedical Materials Research, 2008.

A. Fasoro, D. O. Popa, "Reduced-Order Thermal Analysis of a Packaged Implantable Micropump for Drug Delivery," ASME Journal of Electronic Packaging, (under review) 2008.

Conference papers:

1. Smitha M.N.Rao, Amit Mhatre, Dan O Popa, J. C. Chiao, T. Ativanichayaphong, J. Sin and H.E. Stephanou. "MEMS-based Implantable Drug Delivery System, " in Proc. of TEXMEMS VII Conference, El Paso, Texas, September 2005,
2. Ashutosh Kole, Karishma Bushan, Jeongsik Sin, Woo Ho Lee, Dan Popa, Dereje Agonafer and Harry Stephanou. "Polymer Tube Embedded In-Plane Micropump, " in Proc. of TEXMEMS VII Conference, El Paso, Texas, September 2005.
3. Manan Goel, Harsha Radhakrishnan, Liping Tang, and Hanli Liu, "Application of Near Infrared Multi-spectral CCD Imager to Determine the Hemodynamic Changes in Prostate Tumor, " in proc of Biomedical Optics Topical Meeting, March 19-March 23, 2006, Fort Lauderdale, Florida.
4. Dheerendra Kashyap, Hanli Liu, "Absolute Quantification of Hemoglobin Derivative Concentrations and Reduced Scattering Coefficients from Turbid Media using Steady State Reflectance Spectroscopy with Single Source-Detector Separation, "in proc of Biomedical Optics Topical Meeting, March 19-March 23, 2006, Fort Lauderdale, Florida.
5. Ashutosh Kole, Jeongsik Sin, Woo Ho Lee, Dan Popa, Dereje Agonafer and Harry Stephanou , "Design of Polymer Tube Embedded In-Plane Micropump," ITherm, May 2006.
6. Kole, Ashutosh, Sin, Jeongsik, Lee, Woo-Ho, Popa, Dan, and Agonafer, Dereje, "Polymer Tube Embedded In-Plane Micropump for Low Flow Rate", Proceedings of 24th Digital Avionics Systems Conference, Washington, D.C., October 30 – November 3, 2005
7. Smitha M. N. Rao, Saket Karajigikar, Jeongsik Sin, Dan Popa, Harry Stephanou, J.-C. Chiao, "Progress in the Development of the MEMS-Based In-Plane Micropump: Experimental Motion Characterization", TexMEMS VII Conference, Dallas, October 2006.
8. Manan Goel, Harsha Radhakrishnan, Liping Tang, and Hanli Liu, "Application of Near Infrared Multi-spectral CCD Imager to Determine the Hemodynamic Changes in Prostate Tumor." presented at Biomedical Optics Topical Meeting, Fort Lauderdale, Florida, March 19-23, 2006.
9. D. Kashyap, D. L. Peswani, J. Cadeddu and H. Liu, "Heterogeneities in Concentrations of Hemoglobin Derivatives and Oxygen Saturations in Human Prostate Tumors Evaluated by NIRS," presented at Houston Society for Engineering in Medicine and Biology (HSEMB 2007) February 8, 2007.
10. Dheerendra Kashyap, Nguven Chu, Aditya Apte, BoPing Wang, and Hanli Liu, "Development of broadband multi-channel NIRS (near-infrared spectroscopy) imaging system for quantification of spatial distribution of hemoglobin derivatives," Proc. SPIE Int. Soc. Opt. Eng. 6434, 64341X (2007).

M.S. Thesis and Ph.D Dissertations:

Amit Mhatre, "Implantable Drug Delivery System with an In-Plane Micropump" M.S. Thesis, BioMedical Engineering Department, The University of Texas at Arlington, Arlington, TX, December 2005.

Manan Goel, “Development and Application of Near Infrared CCD Imager to Monitor Hemodynamic Changes in Prostate Tumor During Chemotherapy,” M.S. thesis, BioMedical Engineering Department. The University of Texas at Arlington, Arlington, TX, August 2006.

Dheerendra Kashyap, “Development of a Broadband Multi-Channel Near Infrared Spectroscopic System for Quantifying the absolute Concentrations of Hemoglobin Derivatives,” Ph.D., BioMedical Engineering Department, The University of Texas at Arlington, Arlington, TX, dissertation, May 2007.

Abiodun Fasoro, “Design for Reliability in MicroOptoElectroMechanical Systems (MOEMS)”, Ph.D. Thesis, M.A.E. Dept., The University of Texas at Arlington, Arlington, TX, May 2008.

Invited Talks:

Hanli Liu, “Recent Development on Novel Applications of Optical Spectroscopy and Imaging for Clinical Applications,” Beckman Laser Institute, UC Irvine, Irvine, CA, Sept. 14, 2006.

Hanli Liu, “Non Invasive and Minimally Invasive Characterization of Tumor Using Optical Methods,” Texas Cancer Registry, Texas Department of State Health Services, Mini-Educational Regional Conference, Fort Worth, Texas, July 14, 2006.

Students supported:

Sharman, Vikrant, 3/05 – 5/05

Kashyap, Dheerendra, 07/05 - 08/05

Gorthi, Sankar, 03/05 – 01/06

Radhakrishanan, Harsha, 01/06 - 09/06

Goel, Manan, 03/05 – 09/06

Nair, Ashwin, 01/06 – 01/08

Rao, Smitha, 06/05 – 06/07

Karajgikar, Saket, 09/06-06/07

Prajapati, S, 01/07-06/07

Kaul, Anisha, 06/07-01/08

Fasoro, Abiodun, 06/07-01/08

References

- [1] George Zonios and Aikaterini Dimou, "Modeling diffuse reflectance from semi-infinite turbid media: application to the study of skin optical properties," *OPTICS EXPRESS* Vol. 14(19) 8661-8674 (2006).
- [2] W. B. Wang, J. H. Ali, M. Zevallos, and R. R. Alfano, "Near infrared imaging of human prostate cancerous and normal tissues based on water absorption", in OSA 2004 Biomedical Optics Topical Meetings on CD-ROM (The Optical Society of American, Washington, DC, 2004), MF 38.
- [3] http://www.thermo.com/com/cda/resources/resources_detail/1,2166,13324,00.html
- [4] <http://www.homepages.informatics.ed.ac.uk/rbf/HIPR2/classify.htm>
- [5] Debiotech, S.A., <http://www.debiotech.com/>
- [6] Thomas J. Smith, et. al., "Randomized Clinical Trials of IDDS with CMM for refractory cancer pain", in *Journal of Clinical Oncology*, Vol 20, No 19 (October 1), 2002: pp 4040-4049.
- [7] S. Zafar Razacki, et. al., "Integrated Microsystems for Drug Delivery", in *Advanced Drug Delivery Reviews* 56 (2004) 185– 198
- [8] J. L. Selam, "External and implantable insulin pumps: current place in the treatment of diabetes", in *Exp. Clin. Endocrinol Diabetes* 109 (2001).
- [9] Li Cao, S. Mantell, and D. Polla, "Design and simulation of an implantable medical drug delivery system using MEMS", in *Sensors and Actuators* 94 (2001).
- [10] John T. Santini, et. al., "A controlled-release microchip", in *Nature* Jan 1999.
- [11] Medtronic Minimed <http://www.minimed.com/>
- [12] D J Laser, J G Santiago, " A review of micropumps," *Journal of micromechanics and microengineering*, Vol. 14, 2004.
- [13] Linnemann, P. Woias, C.-D.Senfft, and J.A. Ditterich, " A self-priming and bubble tolerant piezoelectric silicon micropump for liquids and gases," *Proceedings on The Eleventh Annual International Workshop on Micro Electro Mechanical Systems*, pp. 532-537, 1998.
- [14] C. Grosjean and Y.-G. Tai, "A thermopneumatic peristaltic micropump," *International conference on solid state actuators and sensors*, 1999.
- [15] W.L. Bernard, H. Kahn, A.H. Heuer, and M.A. Huff. "Thin-Film Shape-Memory Alloy Actuated Micropumps," *J. MEMS*, Vol. 7, 245, 1998.
- [16] J.G. Smits. "Piezoelectric micropump with microvalves," *Proc. 8th University/Government/Industry Microelectronics Symposium*, 92, 1989.
- [17] J.G. Smits. "Piezoelectric micropump with three valves working peristaltically," *Sensors & Actuators A*, Vol. 21, 203, 1990.
- [18] J.A. Folta, N.F. Raley, E.W. Hee. "Design, fabrication and testing of a miniature peristaltic membrane pump," *5th Technical Digest Solid-State Sensor and Actuator Workshop*, 186, 1992.
- [19] J. Sin, W.H. Lee, H. E. Stephanou, "In-Plane Micropump: design Optimization," *Proc Nanotech*, Vol. 1, 2004.
- [20] Dimitrios K Filippou, Christoforos Tsikkinis, Georgios K Filippou, Athanasios Nissiotis and Spiros Rizos, "Rupture of totally implantable central venous access devices (Intraports) in patients with cancer: report of four cases," *World Journal of Surgical Oncology*, 2004.
- [21] Rubino, R.S.; Gan, H.; Takeuchi, E.S.; "Implantable medical applications of lithium-ion technology," *The Seventeenth Annual Battery Conference on Applications and Advances*, 2002.
- [22] Spillman, D.M.; Takeuchi, E.S.; "Lithium ion batteries for medical devices," *The Fourteenth Annual Battery Conference on Applications and Advances*, 1999.
- [23] J. H. Schulman, J. P. Mobley, J. Wolfe, E. Regev, C. Y. Perron, R. Ananth, E. Matei, A. Glukhovsky, R. Davis, "Battery Powered BION FES Network," *Proceedings of the 26th Annual International Conference of the IEEE EMBS*, 2004
- [24] Akin T, Najafi K and Bradley R M, "A wireless implantable multichannel digital neural recording system for a micromachined sieve electrode," *IEEE Trans. Solid-State Circuits* **33**, 1998.
- [25] Ashutosh Kole, "Polymer Tube Embedded In-plane Micropump: Design, Analysis and Fabrication," Master's Thesis, Univ. of Texas at Arlington, 2005.
- [26] Lisa Brannon-Peppas, "BIOMATERIALS: Polymers in Controlled Drug Delivery," *Medical Plastics and Biomaterials Magazine*, November 1997.
- [27] W.M Saltzman, "Growth factor delivery in tissue engineering," *MRS Bulletin*, 1996.
- [28] Samuel P. Baldwin, W.M Saltzman, "Materials for protein delivery in tissue engineering," *Advanced drug delivery reviews*, 1998.
- [29] "Drug DeliveryMarket Summary," *Nusil Silicone Technology*, White paper.
- [30] J. Urquhart, "Controlled drug delivery: therapeutic and pharmacological aspects," *Journal of internal medicine*, 2000.
- [31] Brian Reilly, Stephen Bruner "Silicones as a Material of Choice for Drug Delivery Applications," NuSil Technology, *Presented at 31st Annual Meeting and Exposition of the Controlled Release Society*, June 12 – 16, 2004.

- [32] Bell, D. J., Lu, T. J., Fleak, N. A., and Spearing, S. M., "MEMS actuators and sensors: observation on their performance and selection for purpose," J. of Micromechanics and Microengineering.15, 2005.
- [33] N. T. Nguyen, and S. Wereley, "Fundamentals and Applications of Microfluidics," Artech house Publication, ISBN 1-58053-343-4, 2002.
- [34] D. Raynerts, "An implantable drug-delivery system based on Shape-Memory-Alloy Micro-Actuation", in Sensors and actuators A61 (1997).
- [35] Huang, Q-A. and Lee, N. K. S., "Analysis and design of polysilicon thermal flexure actuator," J. of Micromechanics and Microengineering.9, 2005.
- [36] A. Grayson, et.al., "Electronic MEMS for triggered delivery", in Advanced Drug Delivery Reviews 56 (2004) 173– 184.
- [37] Guckel, H., Klein, J., Christen, T., Skrobis, K., Lnadon, M. and Lovell, E. G., "Thermo-magnetic metal flexure actuators," Technical Digest IEEE Solid State Sensor and Actuator Workshop, 1992.
- [38] Lin, L. and Chaio, M., "Electrothermal Responses of Lineshape Microstrcutres," Sensors and Actuators A 55, 1996.
- [39] Mhatre, A. "Implantable drug delivery system with an in-plane micropump," Master's Thesis, University of Texas at Arlington, 2005.
- [40] T. J. Farrell, M. S. Patterson, and B. C. Wilson, "A diffusion theory model of spatially resolved, steady-state diffuse reflectance for the noninvasive determination of tissue optical properties *in vivo*," Med. Phys. **19**, 879–888 (1992).
- [41] W. G.Zijlstra, A.Buursma, and V.Assendelft, OW (2000): Visible and near infrared absorption spectra of human and animal haemoglobin (VSP: Utrecht).
- [42] S.J.Matcher and C.E.Cooper, "Absolute quantification of deoxyhaemoglobin concentration in tissue near infrared spectroscopy," Phys. Med. Biol. **39**, 1295–1312 (1994).
- [43] M.Dorigo., V. Maniezzo & A. Colorni, " Ant System: Optimization by a colony of cooperating agents," IEEE Trans. Sys., Man, Cybernetics-Part B, 26(1), 29-41(1986).
- [44] S. Bakhshi, and R. B. North, "Implantable pumps for drug delivery to the brain," Journal of Neuro-Oncology **26** (2) pp 133-139, (1995).
- [45] P. M. Hughes, O. Olejnik, J. Chang-Lin, and C. G. Wilson, "Topical and systemic drug delivery to the posterior segments," Advanced Drug Delivery Reviews **57** (14) pp 2010– 2032 (2005).
- [46] A. Misra, S. Ganesh, and A. Shahiwala, "Drug delivery to the central nervous system: a review," J Pharm Pharmaceut **6** (2) pp 252-273 (2003).
- [47] M. Khoo and C. Liu, "Development of a novel micromachined magnetostatic membrane actuator," IEEE Device Research Conference, pp 109 – 110, June 2000.
- [48] H. Guckel, J. Klein, T. Christenson, K. Skrobis, M. Laudon, and E.G. Lovell, "Thermo-magnetic metal flexure actuators," IEEE Proc., Solid-State Sensor and Actuator Workshop (Hilton Head '92), pp. 73-75, June 1992.
- [49] M. M. Teymoori and E. Ahhaspour-Sani, "A Novel Electrostatic Micromachined Pump for Drug Delivery Systems," Proceedings of IEEE International Conference on Semiconductor Electronics, pp. 105- 109 (2002).
- [50] W. Riethmuller, and W. Benecke, "Thermally Excited Silicon Microactuators," IEEE Trans. Electron Devices, **35** pp 758-763 (1988).
- [51] C.-T. Wu and W. Hsu, "An electro-thermally driven microactuator with two dimensional motion," Microsystem Technologies, **8**, (1) pp 47–50 (2002).
- [52] R. Venditti1, J. S. Lee, Y. Sun and D. Li, "An in-plane, bi-directional electrothermal MEMS actuator," J. Micromech. Microeng. **16**, pp 2067-2070 (2006).
- [53] A. Kole, J. Sin, W. H. Lee, D. O. Popa, D. Agonafer, and H. Stephanou, "Design of polymer tube embedded in-plane micropump," in Proc. of Thermal and Thermomechanical Phenomena in Electronics Systems, 2006. ITherm '06. May 30-June 2, 2006 Page(s):1324 – 1329.
- [54] A. Kole, J. Sin, W. H. Lee, D. Popa, D. Agonafer, and H. Stephanou, " Polymer tube embedded in-plane micropump for low flow rate," Digital Avionics Systems Conference, 2005, DASC 2005. The 24th, Volume 2, 30 Oct.-3 Nov. 2005 Page(s):7 pp. Vol. 2.
- [55] M. Arik, S.M. Zurn, A. Bar-Cohen, Y. Nam, D. Markus and D. Polla, "Development of CAD Model for MEMS Micropumps," Technical Proceedings of the 1999 International Conference on Modeling and Simulation of Microsystems,
- [56] C.D. Lott, T.W. McLain, J.N. Harb and L.L. Howell, "Thermal Modeling of a Surface-micromachined Linear Thermomechanical Actuator," Technical Proceedings of the 2001 International Conference on Modeling and Simulation of Microsystems, Vol. 1, Pages: 370 – 373.
- [57] M.J. Sinclair, A high force low area MEMS thermal actuator, in: Proceedings of the Intersociety Conference on Thermomechanical Phenomena in Electronic Systems, 2000, pp. 127–132.
- [58] L. Que, J. Park, ad Y. B. Gianchandani, "Bent-beam electro-thermal actuators for high force applications," Twelfth IEEE International Conference on Micro Electro Mechanical Systems, 1999. MEMS '99, pp. 31-36.
- [59] Q-H. Huang and N. K. S. Lee, "Analysis and design of polysilicon thermal flexure actuator," J. Micromech. Microeng. **9** (1) pp. 64–70 (1999).

- [60] D. Yan, A. Khajepour and R. Mansour, "Modeling of two-hot-arm horizontal thermal actuator," *J. Micromech. Microeng.* **13** pp. 312–322 (2003).
- [61] C. D. Lott, T. W. McLain, J. N. Harb, and L. L. Howell, "Modeling the thermal behavior of a surface-micromachined linear-displacement thermomechanical microactuator," *Sensors and Actuators A* **101** (1) pp. 239-250 2002.
- [62] Y-J. Yang and C-C. Yu, "Extraction of heat-transfer macromodels for MEMS devices," *J. Micromech. Microeng.* **14** pp. 587–596 (2004).
- [63] C.-C. Lee and W. Hsu, "Optimization of an electro-thermally and laterally driven microactuator," *Microsystem Technologies* **9** (2003) 331–334 2003
- [64] E. S. Kolesar, S. Y. Ko, J. T. Howard, P. B. Allen, J. M. Wilken, N. G. Boydston, M. D. Ruff, and R. J. Wilks, "In-plane tip deflection and force achieved with asymmetrical polysilicon electrothermal microactuators," *Thin Solid Films* **377-378** pp. 719–726 (2000).
- [65] C. H. Pan, C-L. Chang, and Y.-K. Chen, "Design and fabrication of an electro-thermal microactuator with multidirectional in-plane motion," *J. Microlith., Microfab., Microsyst.* **4** (3) 2005.
- [66] S.M. Rao, A. Mhatre, D. O. Popa, J.-C. Chiao, T. Ativanichayaphong, J. Sin, and H.E. Stephanou, "MEMS based Implantable Drug Delivery System," in *Proc. Of TEXMEMS VII*, El Paso, Texas, USA, 2005.
- [67] H. Machiraju, B. Infantolino, B. Sammakia, and M. Deeds, "Thermal Analysis of MEMS Actuator Performance," *Proceedings of IMECE 2007*, Seattle, Washington, USA.
- [68] A Mhatre, "Implantable Drug Delivery System With an In-Plane Micropump." MS Thesis, The University of Texas at Arlington, 2005.
- [69] F.K. Forster, R.L. Bardell, M.A. Afromowitz, N.R. Sharma, and A. Blanchard, "Design, fabrication and testing of fixed-valve micro-pumps," *Proceedings of the ASME Fluids Engineering Division*, pp. 39-44, 1995.
- [70] D. Maillefer, S. Gamper, B. Frehner, and P. Balmer, "A high-performance silicon micropump for disposable drug delivery systems," *The 14th IEEE International Conference on MEMS*, pp. 413-417, 2001.
- [71] Nguyen KT, Shukla KP, Moctezuma M, Braden ARC, Zhou J, Hu Z, Tang L. In vitro studies of the cellular uptake of hydrogel nano- and micro- particles by phagocytes, vascular endothelial and smooth muscle cells. *Journal of Biomedical Materials Research*, 2008.